Monitoring Glial-Restricted Progenitor Cell Survival and Hydrogel Degradation in the CNS of ALS mice

Shreyas Kuddannaya Ph.D.[1], Sarah K. Gross[2], Nicholas J. Maragakis M.D., Ph.D.[2], Jeff W.M. Bulte Ph.D.[1]

[1]Department of Radiology and Radiological Science, Johns Hopkins University SOM, Baltimore, MD, USA,[2]Department of Neurology, Johns Hopkins University SOM, Baltimore, MD

Background: Cell therapies of the central nervous system (CNS) are hampered by high initial cell death and host graft rejection leading to a cell loss of >90% of transplanted cells within 1 week. Diseased environments such as in amyotrophic lateral sclerosis (ALS) can further compromise cell therapy due to high astrogliosis[1].

Objective: We hypothesize that scaffolding cells in composite hyaluronic acid (HA)-based gels can significantly improve transplanted cell survival as evidenced by serial bioluminescence imaging (BLI). Concurrently we aim to assess hydrogel degradation quantitatively via chemical exchange saturation transfer (CEST) MRI due to abundant high amide protons of gelatin[2], without necessitating any exogeneous labels.

Methods: *Cells:* Allogeneic A2B5^{+} murine glial-restricted progenitors (mGRPs) carrying proteolipid protein (PLP-GFP) gene were obtained from fetal forebrain tissue of (E13) transgenic mice and transduced with firefly luciferase (pLenti4-CMV-Luc2) gene. *Gel formulation*: Thiolated HA (HA-S), thiolated gelatin (Gel-S) and poly (ethylene glycol) diacrylate (PEGDA) crosslinker in ratio 2:2:1 were mixed at various concentrations and their rheological properties were optimized. *Transplantation:* A 10 mg/ml gel formulation was chosen and 1.6x10^{5} cells (4x10^{4} cells/site) were transplanted bilaterally in the ventral horns of C3-C4 spinal cord (SC) or the motor cortex (MC) of the SOD1^{G93A} mouse model of ALS via stereotaxic surgery (Figure 1d). MRI was performed on 11.7T horizontal bore Bruker Avance scanner equipped with 15 mm birdcage coil using rapid acquisition and relaxation enhancement (RARE) pulse sequence. *Imaging parameters*: Slice thickness=1.5 mm, Averages= 2, Echo time=19 ms, Relaxation time= 1500 ms, matrix size=128x128, Field of view (FOV)=17x17 mm^2 and RARE factor=16. For CEST imaging, (B1) = 3.6 µT was used with -5.5 to 5.5 ppm offset range.

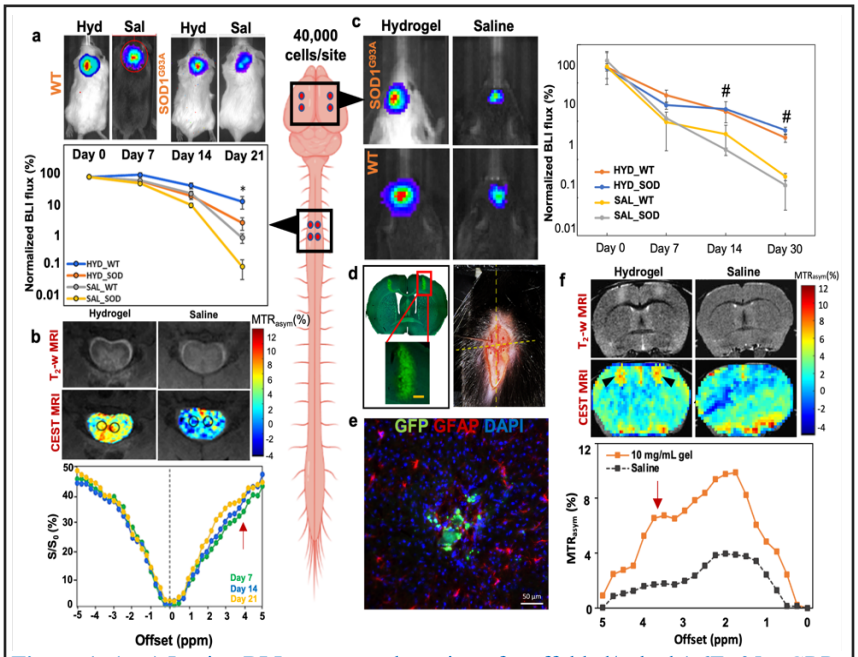

Figure 1: (a, c) In vivo BLI post transplantation of scaffolded/naked 1.6E+05 mGRPs in SC/MC of ALS and WT mice. (*, # p<0.05). (d, e) Transplant site in the motor cortex, with GFP+ cells and anti-GFAP staining (b, f) CEST contrast and T_{2w} MRI at transplanted site validated by z-spectrum or MTR_{asym} curves at 3.6 ppm.

Results: *In vivo* survival of scaffolded vs. naked mGRPs transplanted in SC/MC of the ALS and WT mice was serially monitored by BLI. BLI signal gradually decreased during subsequent weeks in both hydrogel-scaffolded and naked (saline) groups but decreased significantly in the saline group post-day 7 ($p<0.05$) (Fig.1a, c). At endpoint (>4 weeks), scaffolded mGRPs showed significantly higher BLI signal intensity in both MC and SC, accounting for a ~4.5-fold increase in transplanted cell survival compared to naked cells. T_2-w MRI revealed a hyperintense signal at the injection site owing to higher water content of hydrogels. In contrast, the CEST signal was found to be specific for exchangeable protons within the hydrogel and were assessed in terms of *in vivo* MTR_{asym} spectra which revealed two peaks at 0.5–2.0 and 3.6 ppm (Fig.1b, f). Importantly, we noted that the presence of mGRPs in the scaffold (or saline control) did not significantly alter the CEST spectra showing negligible contrast at 3.6 ppm supporting the high specificity of CEST MRI for amide protons in gelatin. Immunohistology with anti-GFAP antibody staining revealed that the activated astrocytes were confined at graft periphery (Fig.1d, e).

Conclusion: Hydrogel morphology and biodegradation were concurrently monitored in a label-free manner via T_2-w MRI and CEST MRI respectively, with hydrogel acting as a barrier for the infiltrating host immune cells. Serial *in vivo* BLI revealed a 4.5-fold enhancement in survival of transplanted allogeneic mGRPs in the CNS. The strategy could be further developed to validate a safe and efficient cell therapy and monitoring for ALS.

References: 1) Srivastava AK, et al. Exp Neurol 2017, 289, 96-102. **2)** Kuddannaya, S, et al. ACS Appl Mater Interfaces 2021, 13 (20), 423-437.

Characterizing the Relationship Between Angiogenesis and Osteogenesis in a Calvarial Defect Model with Multimodality Functional Imaging

Yunke Ren[1], Akanksha Bhargava[2], Janaka Senarathna[2], Xinying Chu[1], Warren Grayson[1-5] and Arvind P Pathak[1,6,7]

Department of Biomedical Engineering[1], Translational Tissue Engineering Center[2], Department of Materials Science and Engineering[3], Department of Chemical & Biomolecular Engineering[4], Institute for Nanobiotechnology[5], Russell H. Morgan Department of Radiology and Radiological Science[6], and Sidney Kimmel Comprehensive Cancer Center[7], Johns Hopkins University, Baltimore, MD, United States

Background:
Remodeling of the vascular microenvironment (VME) is a key factor in bone regeneration that is necessary for the delivery of oxygen, nutrients, inflammatory and bone precursor cells to a defect site. Structural and functional remodeling of the VME includes angiogenesis and concomitant osteogenesis during the first four weeks of bone healing. Although recent advances in optical imaging have elucidated the in vivo relationship between angiogenesis and osteogenesis in a calvarial defect model, these efforts were mostly limited to structural imaging of the vasculature and bone [1].

Objective:
Therefore, the goal of this work is to simultaneously characterize changes in vascular structure and function (i.e. blood flow, oxygenation, etc.) during the bone healing cascade in a mouse calvarial bone defect model.

Methods:
We developed a multicontrast optical imaging framework capable of assessing in vivo changes in: microvascular architecture with intrinsic optical signaling (IOS) imaging; blood flow with laser speckle contrast (LSC) imaging; and bone formation with bright-field imaging, at high spatial (5 μm) and temporal (200 ms) resolutions. With this system we acquired multicontrast images from 10 animals with calvarial defects every 2 days, over 4 weeks **(Fig. 1a, d)**. The bone and vasculature data were then digitally segmented from the bright-field and IOS images for quantitative analysis **(Fig. 1b, c)**. We also euthanized an animal each week for assessing 3D changes in bone volume and vascular architecture using an ex vivo, high-resolution (10 μm) CT imaging workflow we recently developed called VascuViz **(Fig. 1e)** [2].

Results:
Using our in vivo and ex vivo imaging workflow, we demonstrated that angiogenic remodeling within the bone defect microenvironment was robust from post-injury Week 1 to Week 2, during which the microvascular density increased significantly **(Fig. 1f)**. The blood flow exhibited a significant increase at Day 6 (relative to the baseline or Day0) when angiogenesis started, with angiogenic vessels exhibiting maximal perfusion by Day 12 **(Fig. 1d)**. These vascular changes peaked by the end of week 2 and plateaued during the next 2 weeks, which correlated with a significant increase in bone volume during the first 2 weeks, and smaller increase during the last 2 weeks **(Fig. 1f)**.

Conclusions:
Our results indicate that both structural and functional changes in the microvasculature strongly correlated with bone growth during the early stages of calvarial bone healing. Next, we plan to include additional indices of vascular function such as vessel maturity and intravascular oxygenation, as well as to develop image-based hemodynamic models to further characterize the role of the VME during osteogenesis. We believe that this novel imaging framework for characterizing the defect microenvironment can be utilized to inform the design of novel tissue engineering (TE) constructs for craniofacial bone regeneration. Collectively, these advances herald a new era of “image-based TE”.

This work was supported by NIH grants 51R01CA196701-05, 1R01CA237597-01A1 and 5R01DE027957-02.

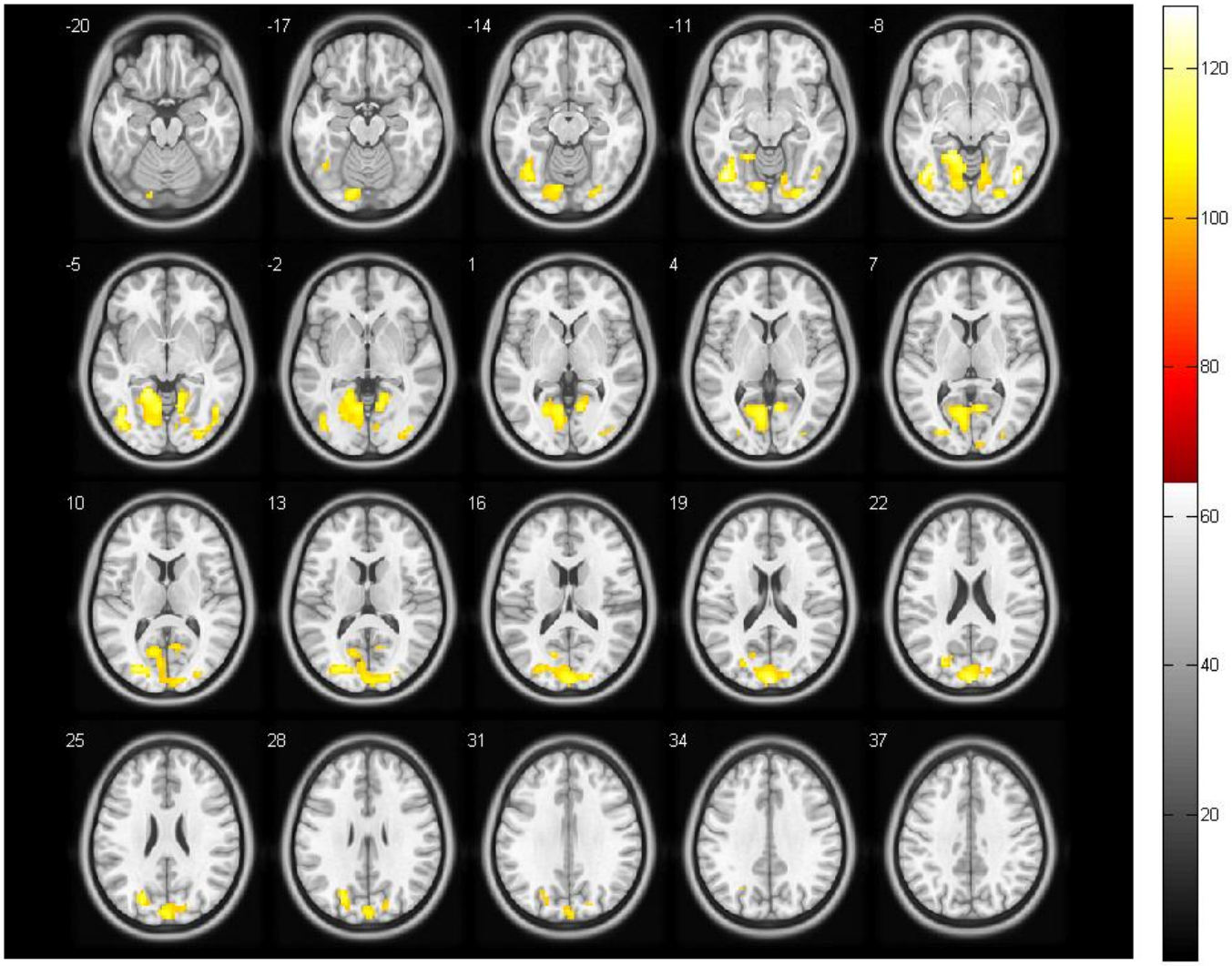

Figure 1 Cerebral areas exhibiting chanMges in ReHo values

Title: Magnetic resonance imaging of ASCT2 transport in a mouse model of prostate cancer

Authors: Behnaz Ghaemi[1,2], Yuguo Li[3], Martin G. Pomper[1], Jeff W.M. Bulte[1,2], Peter C.M. van Zijl[1,3], Aline M. Thomas[1,2]

[1]The Russell H. Morgan Department of Radiology and Radiological Science, School of Medicine, Johns Hopkins University, Baltimore, MD; [2]Cellular Imaging Section and Vascular Program, Institute for Cellular Engineering, Johns Hopkins School of Medicine, Baltimore, MD; [3]F.M. Kirby Center for Functional Brain Imaging, Kennedy Krieger Institute, Baltimore, MD.

Background: Alanine serine cysteine transporter 2 (ASCT2) is a prognostic marker for many cancers[1-3]. Alanine is an ASCT2 substrate[4] that can be detected using chemical exchange saturation transfer (CEST) MRI through the exchange of its amine protons with water protons[5].

Objective: We evaluated the utility of CEST MRI to monitor ASCT2-mediated transport by comparing DU-145 and LNCaP prostate cancer cells, which have different levels of ASCT2 expression[6, 7].

Methods Prostate cancer model: Animal studies were approved by the ACUC of Johns Hopkins University. DU-145 (2-3 x 10^6; n=4) or LNCaP (3-5 x 10^6; n=4) cells were subcutaneously injected into the right flank of male, 6-10 week old Rag2 mice (Jackson Laboratories). CEST MRI: Mice were imaged 1-2 months after tumor induction using a Bruker 11.7T horizontal bore spectrometer and an 8-channel phase array coil. Animals were anesthetized with isoflurane (1-2%). CEST images were collected at the +3.1 ppm frequency at baseline and over a period of 60 minutes after alanine (6 mM, IV) injection. CEST enhancement ($\Delta S/S_{0,0\text{-}t}$) was quantified by subtracting the signal (S/S_0) at time t from the signal obtained prior to injection. S_0 was acquired before and after (n = 5 each), then linearly fitted over time to correct for thermal drift. Scan parameters were TR/TE = 10000/3.49 ms, RARE factor = 32, NA = 20, repetitions = 1, B_1 = 3.6 μT, saturation length = 3 s, matrix size = 48 x 48, slice thickness = 1.5 mm, and field of view = 30 × 30 mm^2.

Results When alanine was administered into mice with DU-145 tumors, CEST signal was near or below baseline levels throughout the scan (**Figure 1**). When alanine was administered into mice with LNCaP tumors, CEST signal at the +3.1 ppm frequency was enhanced after injection throughout the 60-minute scan. CEST signal was significantly higher than that in DU-145 tumors at 60 minutes (p=0.012).

Conclusions CEST MRI detected the uptake of alanine, a natural ASCT2 substrate. CEST enhancement distinguished prostate tumors with differing ASCT2 levels.

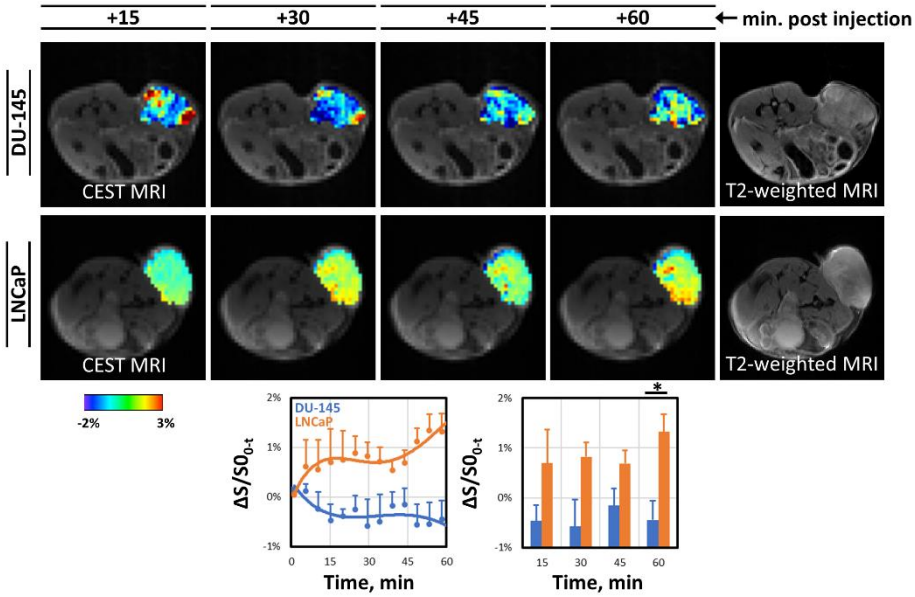

References

1. Sun, H.-W., et al., PLOS ONE, 2016. **11**(12): p. e0168907.
2. Shimizu, K., et al., British Journal of Cancer, 2014. **110**(8): p. 2030-2039.
3. Bernhardt, S., et al., Breast Cancer Research, 2017. **19**(1): p. 112.
4. Foster, A.C., et al., PLOS ONE, 2016. **11**(6): p. e0156551.
5. Chen, J., et al., NMR in Biomedicine, 2020. **33**(1): p. e4188.
6. Wang, Q., et al., The Journal of Pathology, 2015. **236**(3): p. 278-289.
7. Cardoso, H.J., et al., Cellular Oncology, 2021. **44**(2): p. 385-403.

Figure 1. CEST MRI in prostate tumors. Visualization of CEST signal enhancement at the +3.1 ppm frequency upon alanine injection in DU-145 (Top; n=4) and LNCaP (Middle; n=4) tumors. T2-weighted images are shown for reference. (Bottom) Quantification of enhancement in tumors over the course of the scan.

The usefulness of various Prostate-specific membrane antigen (PSMA) ligands labeled with radionuclides in the diagnosis and treatment of metastatic prostate cancer

[1]Shashi B Singh, MBBS, [1]Bimash B Shrestha, MBBS, [1]Rajendra P Shah, MD, [1]Sahith Valluru, MBBS, [1]William Y Raynor, MD
[1]Department of Radiology, Hospital of the University of Pennsylvania, Philadelphia, USA

Background: Prostate cancer is the second most common cancer in men and the fifth most common cause of death worldwide. Current treatment options for prostate cancer include radical surgical resection, radiotherapy, chemotherapy, targeted therapy, immunotherapy, and androgen deprivation therapy. Androgen deprivation therapy is the most effective against advanced prostate cancer. However, after 1 to 2 years of androgen sensitivity, the majority of patients will become castration-resistant which may hasten the progression of the disease, accelerate prostate cancer metastasis, and finally proceed to metastatic castration-resistant prostate cancer (mCRPC). This renders chemotherapy and castration treatment useless. There are still no effective treatments for mCRPC patients. However, PSMA ligands labeled with radionuclides have been employed in the diagnosis and treatment of prostate cancer in recent years, with encouraging results. After FDA approved ^{68}Ga-PSMA in 2020, the first PSMA-based PET tracer, for patients with prostate cancer who had a biochemical recurrence, other PSMA-based radiotracers with further benefits have become available since then. However, research into their relative usefulness is lacking.

Objectives: To explore the usefulness, relative efficacy, and safety of PSMA PET tracers in the diagnosis and treatment of prostate cancer.

Methods: The search terms “prostate cancer”, “PSMA”, and “theranostic’’ were used to curate studies indexed by PubMed and Google Scholar in order to compile a comprehensive literature review. Highly cited articles were reviewed to evaluate PSMA PET tracers with respect to their usefulness, efficacy, and safety.

Results: FDA approved ^{68}Ga-PSMA-11 and ^{18}F-DCFPyL (Pylarify) for patients with prostate cancer. Effective in diagnosis of prostate cancer as their positron emission identified by PET imaging. When compared to CT or MRI alone, gallium 68 (^{68}Ga)–PSMA-11 PET has improved diagnostic accuracy for detecting recurrent prostate cancer. Other PET radiotracers, such as fluorine-18 (^{18}F) fluorocholine and carbon-11-choline, also underperform in comparison to gallium 68 (^{68}Ga)–PSMA-11.

The most extensively used PSMA-targeted endoradiotherapy/radioligand therapy (PRLT) agents are beta-particle-emitting tracers, such as ^{177}LuPSMA-617 and ^{177}Lu-PSMA-I&T (imaging and treatment). The ^{177}Lu emits low-energy gamma photons that can be employed in diagnostics and moderate-energy beta particles that can be used in treatment. Both ^{177}Lu-PSMA-617 and ^{177}Lu-PSMA-I&T have similar biodistribution and efficacy. As a result, the recent guidelines consider these tracers interchangeable in practice and recommend that PRLT be considered among men with mCRPC who have failed or are not eligible for the standard of care management, provided that they have adequate uptake of a PSMA-targeted radiotracer on a prior PET scan. The ^{177}Lu-PSMA-617 has demonstrated good efficacy, safety, ease of availability, and high therapeutic value. However, the majority of patients become non-responsive to ^{177}Lu treatment later, with subsequent worsening of their conditions. Similarly, in a meta-analysis done to evaluate the efficacy and safety of ^{225}Ac-PSMA-617, the pooled proportions of patients with decreased PSA and PSA decreased by more than 50% were 87.0% and 66.1%, respectively. More than half of the patients had molecular responses. Treatment with ^{225}Ac-PSMA-617 significantly improved health-related quality of life including physical symptoms such as pain, difficulty urinating, fatigue, and limited physical activity. The ^{225}Ac-PSMA-617 targeted therapy for prostate cancer patients has a strong therapeutic impact with minimal side effects for mCRPC patients. ^{225}Ac-PSMA-617 is still in the clinical trial stage, and the efficacy and safety of its treatment plan, if assessed in a high-quality, multi-center, prospective multi-arm randomized controlled trial, may be very useful. Similarly, a continuous follow-up study is needed to see if patients who lack or have poor PSMA expression can still benefit from PSMA RLT and how to choose a suitable and effective combo therapy plan.

Conclusions: The FDA's approval of two ^{68}Ga-based PSMA targeting agents has prepared the way for a ^{177}Lu PSMA targeting agent to be approved in the future. In the future, randomized controlled trials assessing the therapeutic effects and survival benefits of various PSMA-targeted radioligands compared to those of existing clinical treatments and their relative efficacy may help us better understand their optimal clinical utility.

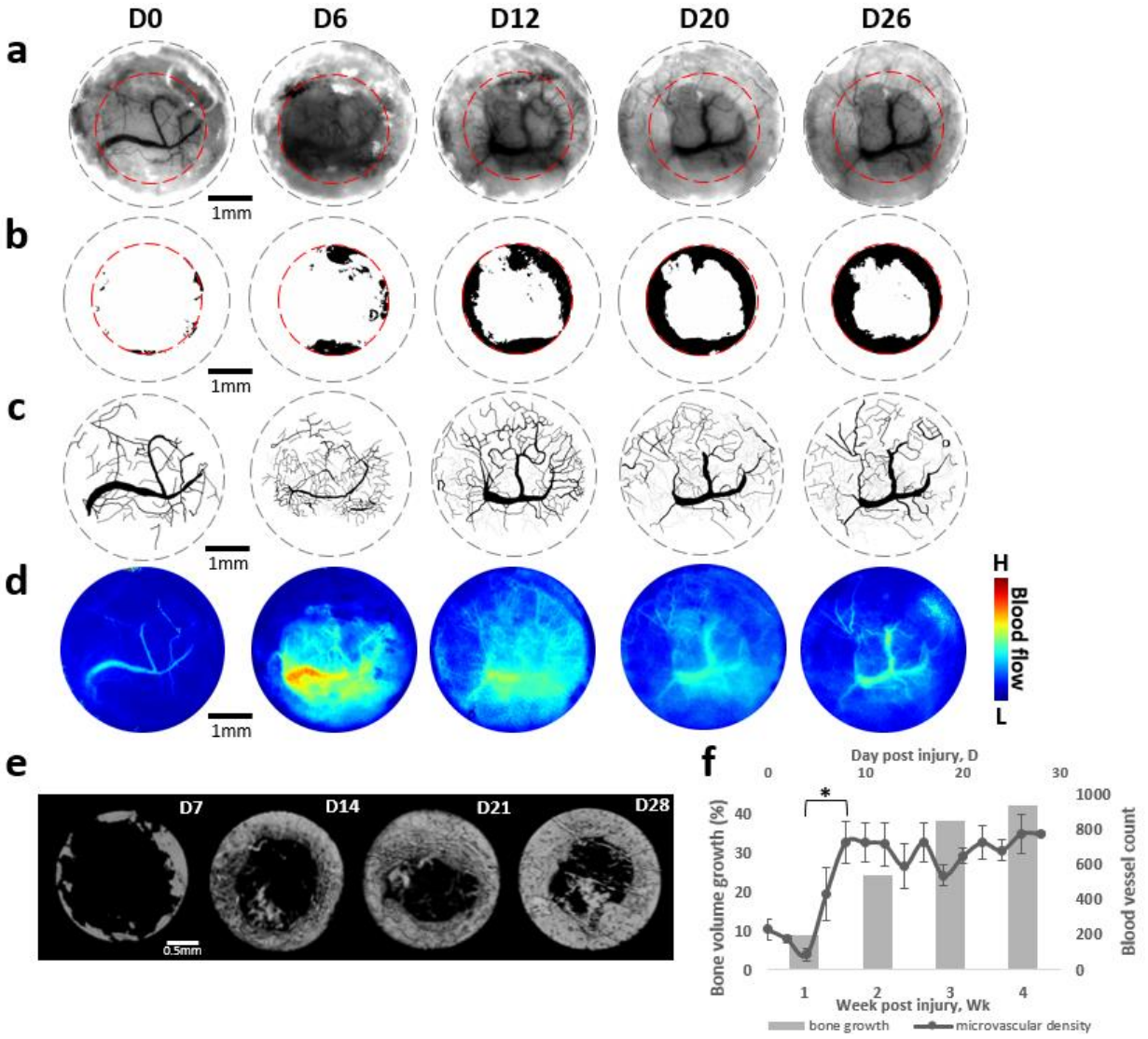

<u>Fig. 1: Multicontrast in vivo imaging in a calvarial defect model over 4 weeks (D0-D26).</u> (**a**) Representative Intrinsic Optical Signal (IOS) images acquired at 5µm resolution showing bone and vessel morphology. Grey dashed lines represent the field-of-view (FoV) visible through a 3mm diameter cranial window. Red dashed lines represent the 2 mm diameter calvarial defect. (**b**) Semi-automatic segmentation of bone using *Ilastik*, a machine-learning based image segmentation tool, illustrates robust osteogenesis from D6-D26. (**c**) Manual segmentation of blood vessels illustrates angiogenesis within the defect over 4 weeks; and (**d**) Laser Speckle Contrast (LSC) images illustrate the concomitant changes in blood flow during bone healing. (**e**) Ex vivo CT images of bone volume within the defect acquired using our "VascuViz" protocol [2] illustrate robust osteogenesis from D7-D28. (**f**) Correlation between in vivo changes in microvascular density and ex vivo measurements of bone growth during bone healing over 4 weeks. Each data point represents mean ± SEM (n=3). *Significant difference ($p<0.05$).

References:

[1] Huang, C., Ness, V. P., Yang, X., Chen, H., Luo, J., Brown, E. B., & Zhang, X. (2015). Spatiotemporal Analyses of Osteogenesis and Angiogenesis via Intravital Imaging in Cranial Bone Defect Repair. *Journal of bone and mineral research : the official journal of the American Society for Bone and Mineral Research*, *30*(7), 1217–1230. https://doi.org/10.1002/jbmr.2460

[2] Bhargava, A., Monteagudo, B., Kushwaha, P. *et al.* VascuViz: a multimodality and multiscale imaging and visualization pipeline for vascular systems biology. *Nat Methods* **19,** 242–254 (2022). https://doi.org/10.1038/s41592-021-01363-5

The radionuclide evaluation of morphological changes in the bone tissue with delayed union.

G. Qiao[1], S.A. Lepekhova[2], O.A. Goldberg[3], I.S. Kurganskii[3], T.M. Andaeva[4]

[1] Department of Diagnostic Radiology and Nuclear Medicine, School of Medicine, University of Maryland at Baltimore

[2] Irkutsk Scientific Center of Siberian Branch of the Russian Academy of Sciences

[3]Irkutsk Scientific Center of Surgery and Traumatology

[4] Irkutsk Regional Clinical Hospital

Background. The physiology of bone regeneration is a complex process. Definition of delayed or nonunion and end points of bone formation are most meaningful. Bone scintigraphy is a quick and sensitive radionuclide procedure. Bone scintigraphy during reparative regeneration can evaluate blood flow and the rate of new bone formation, which defines phases of regeneration.

Objective. The radionuclide evaluation of morphological changes in the bone tissue with delayed union.

Methods. The study performed on laboratory animals (rabbits, 6 mo., 3 kg). All the experimental animals underwent modeling of delayed bone union with radionuclide and morphological evolution. The technique of bone scintigraphy is IV injection of phosphate and bisphosphonate compounds radiolabeled with technetium-99^m (2.5 μCi/kg) for evaluation of morphofunctional changes in the bone with delayed union.

Result. The delayed union of bone fragments by day 14 was established to lead to marked morphological changes in by day 20, with pseudoarthrosis formation by day 50. As it was established by bone scintigraphy technique, evolution of radionuclide accumulation in the zone of bone regeneration increased in dynamic stage – perfusion in the bone regeneration and static stage – accumulation radionuclide, thereby evidencing of the maintaining active reparation processes up to day 50. Histological study shows the formed cavities revealed the walls of which were formed with hyaline cartilage, with observed enchondral ossification of callus underlying spongy bone, with collagen fiber foci and sites of spongy bone structure. The predominance of connective cartilaginous tissue and bone tissue ratio was 1:1.

Conclusions. The scintigraphy established an increase in the amount of accumulation of the radionuclide in the zone of bone regeneration in dynamic and static stage of bone scintigraphy by more than 2 times compared with the normals ($p \leq 0.01$), which indicates the maintenance of inflammatory changes in the soft tissues and the incompleteness of the bone formation process and lead to pseudoarthrosis formation by day 50 of the study.

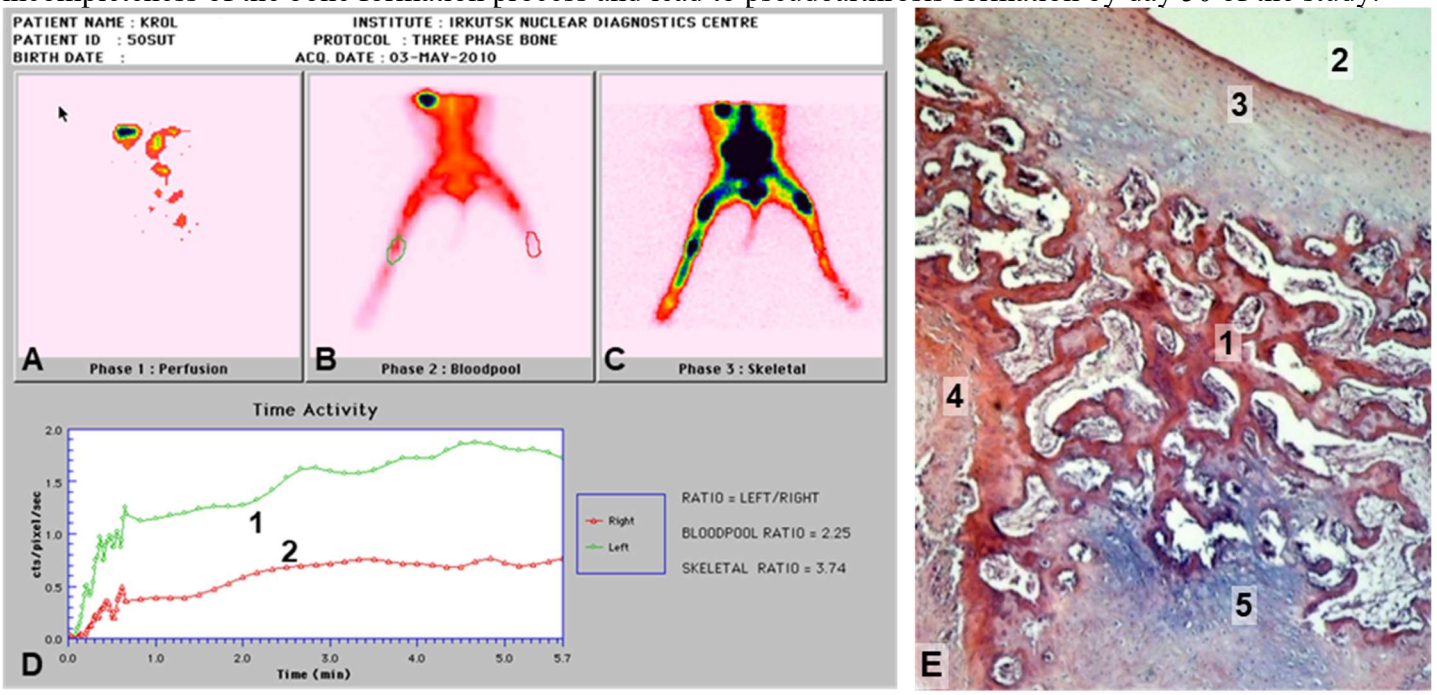

Figure. Radionuclide and morphological evaluation of delayed bone regeneration. A – perfusion stage; B – blood pool (dynamic) stage; C – skeletal (static) stage; D – time activity curves: 1 – area with delayed regeneration, 2 – contralateral side; E – Hematoxylin and eosin staining of bone regeneration area (80x) at day 50: 1 – cancellous bone, 2 – cavity, 3 – hyaline cartilage, 4 – collagen fibers, 5 – chondrocytes.

Quantitative cerebrovascular reactivity MRI in mice using acetazolamide challenge

Zhiliang Wei, PhD[1,2], Yuguo Li, PhD[1,2], Xirui Hou, PhD[3], Zheng Han, PhD[1,2], Jiadi Xu, PhD[1,2], Michael T. McMahon, PhD[1,2], Wenzhen Duan, PhD[4,5], Guanshu Liu, PhD[1,2], Hanzhang Lu, PhD[1,2,3]

[1] Department of Radiology, Johns Hopkins School of Medicine, Baltimore, MD, USA. [2] F. M. Kirby Research Center, Kennedy Krieger Research Institute, Baltimore, MD. [3] Department of Biomedical Engineering, Johns Hopkins School of Medicine, Baltimore, MD. [4]Department of Psychiatry and Behavioral Sciences, Johns Hopkins School of medicine, Baltimore, MD. [5]Department of Neuroscience, Johns Hopkins School of medicine, Baltimore, MD.

Background: Cerebrovascular reactivity (CVR) is a sensitive marker for various neurovascular diseases[1,2] and is often measured with hypercapnia challenge in human studies.[3] However, hypercapnia method is not applicable for mice due to the difficulty in quantifying end-tidal CO_2 level of the exhaled gas.

Objective: We aimed to develop a method for evaluating quantitative CVR in small animals.

Methods: The pharmaceutical challenge of acetazolamide (ACZ) was utilized and plasma ACZ concentration was measured with high-performance-liquid-chromatography (HPLC) to quantify stimulus (Fig. 1A). To confirm that the observed vascular response is attributed to ACZ injection rather than other factors such as time-dependent changes in anesthesia level or hemodilution effect of fluid injection, we compared the result of ACZ injection with those of phosphate-buffered saline (PBS) injection and no injection (N=5; Study 1). Dose dependence (30, 60, 120 and 180 mg/kg) of vascular responses on ACZ was also investigated (N=5; Study 2). Both global (by phase-contrast, PC MRI[4]) and regional (by pseudo-continuous arterial-spin-labeling, pCASL MRI[5]) CVR measurements were demonstrated (N=4; Study 3).

Results: <u>*Study 1*</u>: Vascular response to ACZ was characterized by a sharp build up in <10 min (data not shown). There was a significant difference in averaged CBF changes among ACZ injection, PBS injection, and no injection (Fig. 1B, P=0.0001), suggesting that ACZ was a primary factor of CBF increase. <u>*Study 2:*</u> The averaged CBF changes revealed an absence of difference (Fig. 1C, ANOVA: P=0.50) among doses ≥30mg/kg, suggesting that further increasing dose >30 mg/kg did not provide additional benefit to the detection of vascular response. HPLC revealed a linearity between injection dose and plasma ACZ concentration ($[ACZ]_{plasma} = 1.04dose, R^2 = 0.76, P < 0.0001$). <u>*Study 3:*</u> Figure 1E shows group averaged CBF map of a representative slice during pre- and post-injection periods at multiple PLDs. Visual inspection suggested that CBF was increased throughout the brain due to ACZ administration at all PLDs. There was not an effect of PLD on CVR (data not shown, P=0.94). In general, across different regions, cerebral cortex (CVR=0.68±0.18%/[μg/ml]) manifested a higher CVR compared to deep brain regions (e.g. CVR=0.34±0.09%/[μg/ml] for striatum).

Finally, none of the mice studied showed aberrant behaviors or appearance over a minimum of 6 months after the final MRI scan, supporting the safety of ACZ injection in CVR MRI.

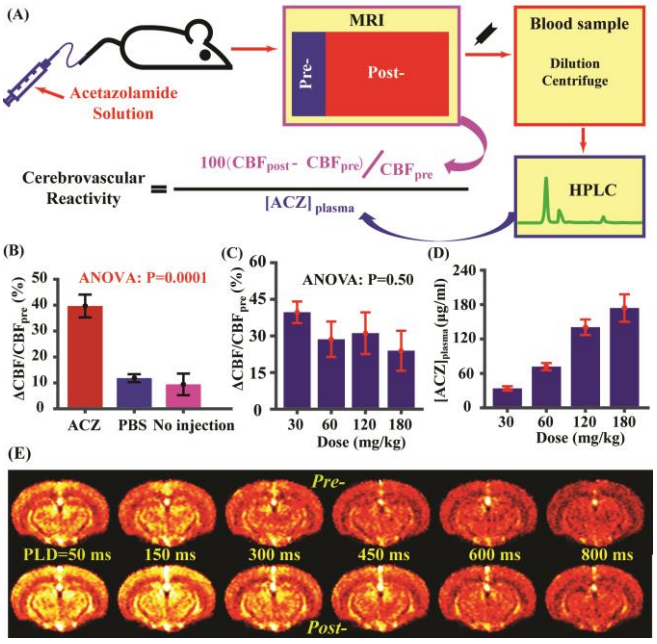

Figure 1 ACZ-challenge-based CVR MRI in mouse. (A) Schematic diagram of procedures; cerebral blood flow, CBF; (B) vascular response at different injections (Study 1); (C) vascular response at different ACZ doses (Study 2); (D) dependence of plasma ACZ level on injection dose revealed by HPLC; (E) perfusion map of a representative slice at pre- and post-injection with multiple post-labeling delays (PLD).

Conclusions: We developed a quantitative CVR method in mice using ACZ challenge. Evidences of feasibility, safety, temporal characteristics, spatial resolution, and dose-dependence of the acetazolamide-based CVR technique have been demonstrated, thus providing a quantitative tool for assessing vascular reactivity in mice.

References: 1. Sur S *et al.* Neurology (2020) 95:e962-e972. 2. Liu P *et al.* Radiology (2021) 299:419-425. 3. Liu P *et al.* NeuroImage (2019) 187:104-115. 4. Wei Z *et al.* Magn Reson Med (2019) 81:2566-2575. 5. Hirschler L *et al.* Magn Reson Med (2018) 79:1314-1324.

Acupuncture at SP3 in healthy volunteers affects cerebral areas: An explorative resting-state fMRI study

Feng Wang MD, PhD[1], Tiansong Yang PhD[1], Xiaoling Li[1], Xiaohui Liu[2], Danna Cao[1], Delong Wang[2], Yan Yang[2], Chaoran Li[2], Yuanyuan Qu[2], Xu Zhao[1], Li Ying Kathy Diao MS, L.Ac.[5], Zhongren Sun PhD[2], Tetsuya Asakawa[3,4]

1First affiliated hospital, Heilongjiang University of Chinese Medicine, Harbin, China

2Heilongjiang University of Chinese Medicine, Harbin, China

3Department of Neurosurgery, Hamamatsu University School of Medicine, Hamamatsu, Japan

4Research Base of Traditional Chinese Medicine Syndrome, Fujian University of Traditional Chinese Medicine, Fuzhou, China

5Liying Acupuncture Healing Services, LLC, Columbia MD 21046 USA

Background

Acupuncture is an ancient therapeutic modality based on theories of Traditional Chinese Medicine (TCM) in which the mechanisms are multifold and not fully understood. It is currently gaining popularity as an important modality of alternative and complementary medicine in the western world. Modern neuroimaging techniques such as functional magnetic resonance imaging, positron emission tomography, and magnetoencephalography provides a new vision of the neurobiological foundations of acupuncture. As a nonspecific physical stimulation, the effect of acupuncture on diseases is produced by motivating the inherent regulatory system in the body, having the characteristics of whole regulation, dual directional regulation, etc. Recently resting-state functional magnetic resonance imaging (rsfMRI) has become an important research and diagnostic method to show the mechanisms on how acupuncture works. The values of regional homogeneity (ReHo) were also used for exploring the changes in cortical functional regions.

Objective

In this study, we aimed to explore the short-term effects of acupuncture on cerebral areas with changes in regional homogeneity (ReHo) induced by effective unilateral acupuncture on the Taibai (SP3) point in healthy subjects.

Methods

In the study, randomized, crossover design was used. Fifteen healthy right-handed volunteers (age: 20–35 years) participated. A 3.0T magnetic resonance imaging (MRI) system was used to perform resting-state functional MRI scan after unilateral (right side) sham and effective acupuncture on the SP3 point (15 minutes applied with “Deqi” reaction). The differences in cerebral ReHo values between post-effective acupuncture and post-sham acupuncture were compared using the SPM 12 software.

Results

Post-effective acupuncture of SP3 compared with post-sham acupuncture, the brain area with decreased ReHo values were bilateral BA18, cuneus, and BA17, along with BA41, BA22, postcentral gyrus, and BA7 on the right side.

Conclusions

The ReHo method has been assessed in terms of evaluating altered resting-state properties and for providing evidence of functional changes in healthy volunteers with acupuncture stimulation. The results reveal that most dominant cerebral areas affected by SP3 acupuncture were bilateral visual-related cortices (lingual gyrus, cuneus, and calcarine), along with the unilateral postcentral gyrus and superior parietal lobule. These findings may provide more further clinical and experimental potential explanations concerning the efficacy of SP3 acupuncture.

Keywords: acupuncture, regional homogeneity, resting-state functional magnetic resonance imaging, Taibai (SP3)

MOST MRI: label-free detection of cationic compounds by their proton exchange modulating effect

Zheng Han[1,2,3], Safiya Aafreen[1,2,4], Yang Zhou[1,2], Chongxue Bie[1,2], Jiadi Xu[1,2], Peter van Zijl[1,2], Guanshu Liu[1,2]
1 F.M Kirby Center, Kennedy Krieger Institute, 2 Department of Radiology, Johns Hopkins University, 3 Health Sciences Center, University of Oklahoma; 4 Department of Biomedical Engineering, Johns Hopkins University

Background: Chemical exchange saturation transfer (CEST) MRI is an emerging technology(Ward et al. 2000), which has allowed detecting various diseases using endogenous CEST agents including proteins and metabolites. The CEST contrast is predominated by both the concentration and exchange rate of a given CEST agents, with the latter sensitive to various environmental factors.(Liepinsh and Otting 1996) Herein we successfully developed a novel contrast mechanism to detect vectors by their effect on the exchange rates of CEST agents (**Fig. 1A-C**), namely Modulated Saturation Transfer (MOST) MRI. We demonstrated that MOST can be used to label-free detect cationic polymer PEI, providing a theranostic MRI technology that can be seamlessly integrated into most cationic polymer-based gene therapy(Zakeri et al. 2018).

Objective: To establish MOST MRI for label-free detection of cationic polymers and theranostic gene therapy.

Methods: In vitro phantom studies were carried out using a 9.4 T vertical bore Bruker MRI scanner according to our published procedures.(Chan et al. 2012) C57BL/6J mice were inoculated with syngeneic $Kras^{LSL.G12D/+}$; $p53^{R172H/+}$; $Pdx^{Cretg/+}$ (KPC)-derived PDAC cells subcutaneously into their lower flanks(Han et al. 2019). After 2 weeks, PEI polymers were intratumorally injected (50 µg per mouse) and CEST MRI was conducted pre and 10 minutes post- injection.

Results: Our data showed that, while PEI600 itself carries no CEST signal (**Fig. 1D**), it exerts a strong quenching effect on the CEST contrast of D-Glucose (**Fig. 1E**). Such an effect (MOST contrast) could be observed as low as 4 µg/mL (13 µM) PEI600. When demonstrated in the pancreatic cancer mouse model, 50 µg PEI resulted in an average -57.9% change in the endogenous CEST in tumors **(Fig. 1F).**

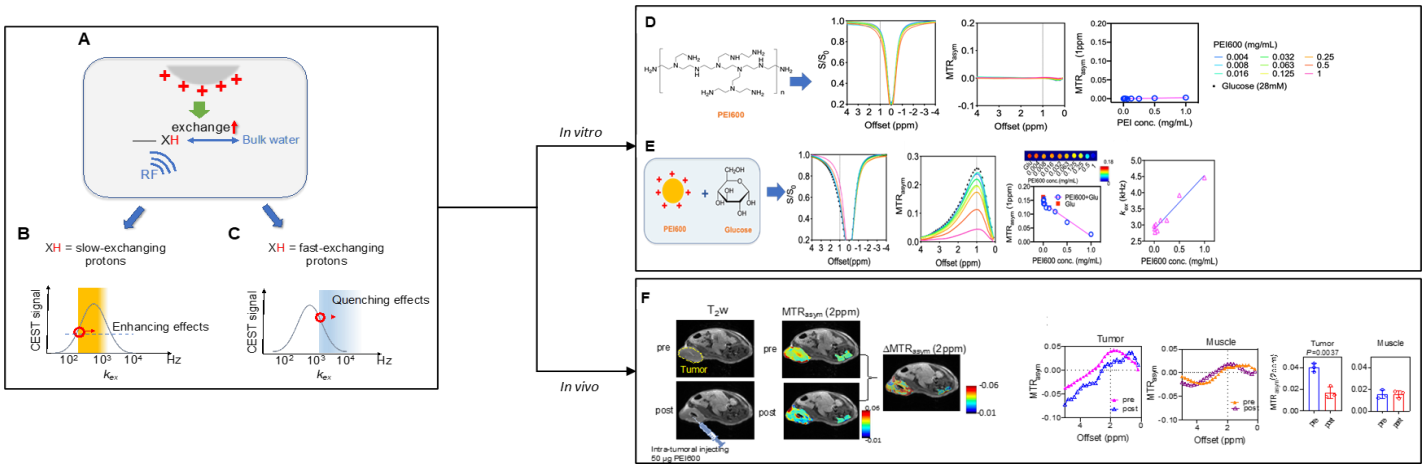

Figure 1. Schematic summary of mechanism and supporting in vivo and in vitro results. A. Cationic compounds are known to modulate the proton exchange process. **B.** For slowly exchanging protons, increasing the exchange rate will enhance the CEST contrast. **C.** For intermediate exchanging protons, increasing the exchange rate more and more will lead to a quenching effect on the CEST signal. **D.** Phantom results of Z-spectra, MTR_{asym} plots and mean MTR_{asym} (1ppm) values of PEI600 at different concentrations ranging from 0.004 to 1 mg/mL. **E.** Quenching effect of PEI600 on the CEST signal of D-glucose das shown in Z-spectra and MTR_{asym} plots, MTR_{asym}(1 ppm) colormaps of D-glucose(28mM)+PEI (0.04 to 1 mg/mL) phantoms, showing dose-dependent decrease in CEST signal with PEI600 concentrations and Scatter plot Exchange rates of D-glucose increase linearly with PEI600 concentrations. **F.** MRI tracking of intratumorally injected PEI600 with T2w and MTR_{asym} (2 ppm) maps showing the injection site and decreased MTR_{asym} signal in the tumor with change in ΔMTR_{asym} (2 ppm) maps showing a significantly higher decrease in tumor compared to muscle, MTR_{asym} plots (mean values of three tumors) and comparison of the change of MTR_{asym} (2 ppm values) (D) of tumor and muscle.

Conclusion: MOST MRI detected cationic compounds such as PEI by their proton exchange modulation of CEST agents. This method is sensitive and allows theranostic MRI of gene therapy in a label-free manner.

Funding Support: R01CA211087

References: Ward KM, Aletras AH, Balaban RS (2000). J Magn Reson 143 (1):79-87; Liepinsh E, Otting G (1996). Magn Reson Med 35 (1):30-42; Zakeri A, Kouhbanani MAJ, Beheshtkhoo N et al. (2018). Nano Rev Exp 9 (1):1488497; Chan KW, McMahon MT, Kato Y et al. (2012). Magn Reson Med 68 (6):1764-1773; Han Z, Zhang S, Fujiwara K et al. (2019). Bioconjug Chem 30 (5):1425-1433

Abnormal Brain Diffusivity in Participants with Persistent Neuropsychiatric Symptoms after COVID-19

Huajun Liang[1] MBBS, PhD, Thomas Ernst[1,2] PhD, Kenichi Oishi[3] MD, PhD, Meghann Ryan[4] MA, Eleanor Wilson[5] MD, Andrea Levine[6] MD, Eric Cunningham[1] BS, Shyamasundaran Kottilil[5] MD, PhD, Linda Chang[1,2,7] MD

[1]Diagnostic Radiology and Nuclear Medicine, University of Maryland School of Medicine, Baltimore, MD, United States.[2]Department of Neurology, Johns Hopkins University School of Medicine, Baltimore, MD, United States. [3]Department of Radiology, Johns Hopkins University School of Medicine, Baltimore, MD, United States. [4]Program in Neuroscience, University of Maryland School of Medicine, Baltimore, MD. [5]Institute of Human Virology, Department of Medicine, Division of Infectious Disease, University of Maryland School of Medicine, Baltimore, MD, United States. [6]Department of Medicine, Division of Pulmonary & Critical Care Medicine, University of Maryland School of Medicine, Baltimore, MD, United States. [7]Department of Neurology, University of Maryland School of Medicine, MD, United States.

Corresponding author: Linda Chang, 670 W. Baltimore Street, HSF III, Baltimore, MD 21201, USA. Email: LChang@som.umaryland.edu

Background Neuropsychiatric symptoms associated with post-acute sequelae of COVID-19 (PASC) are common during convalescence. Abnormal brain white matter integrity was reported at 2-3 months after acute infection in those who recovered from COVID-19, but these studies did not specifically evaluate those with neuropsychiatric symptoms.

Objectives To understand whether brain microstructural abnormalities contribute to the PASC.

Methods Cognitive performance, psychiatric symptoms (NIH Toolbox® and PROMIS) and diffusion tensor imaging (DTI) metrics were compared for 23 participants with PASC (15 women, average age=44.1±2.5 years, 158 days since COVID-19) and 24 uninfected controls (13 women, average age=44.3±2.6 years). Fractional anisotropy (FA), axial (AD), radial (RD), and mean (MD) diffusivities were assessed using MRICloud with an automated Multi-atlas label fusion method to evaluate 9 white matter and 6 subcortical brain regions.

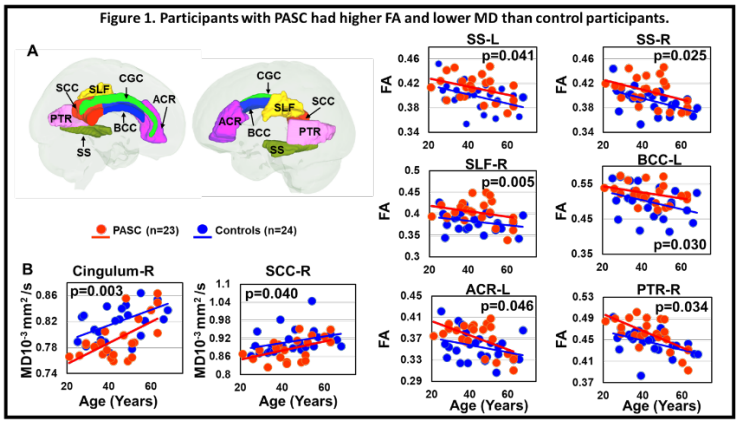

Figure 1. Participants with NPASC had higher FA and lower MD than control participants. A) Brain regions showing significant group differences. **B)** Participants with PASC had lower MD than controls in the right cingulum (CGC) and the right splenium of corpus callosum (SCC). **C)** Participants with PASC had higher FA than controls in bilateral sagittal strata (SS), right superior longitudinal fasciculus (SLF), left body of corpus callosum (BCC), left anterior corona radiata (ACR), and right posterior thalamic radiation (PTR). PASC: participants with post-acute sequelae SARS-CoV-2 infection, FA: Fractional anisotropy, MD: mean diffusivity, R: right side, L: left side.

Results The median time since COVID-19 diagnosis was 158 days (range: 42-399 days). PASC and control participants were similar in age, proportions of sex and race, education level, and socioeconomical status. The most common neuropsychiatric symptoms reported by the PASC group were difficulty with concentration (87%), fatigue (83%), and memory (79%). However, the PASC group tended to have a higher body mass index (+13.4%, p=0.056) than controls.

Compared to controls, PASC had similarly normal cognitive performance, but greater psychiatric symptoms and perceived stress, higher FA, and lower diffusivities in multiple white matter tracts on the right and few on the left (ANCOVA-p-values=0.007-0.051). Women with PASC had higher left amygdala-MD compared to control women (p=0.010), but no difference in men (Sex-by-PASC-p=0.005). Higher sagittal strata-FA predicted greater fatigue in all participants (r=0.515, p<0.001), while lower corpus callosum-FA predicted more pain interference in PASC (r=-0.557, p=0.006). Regardless of COVID-19 status, higher MD in the left amygdala predicted greater fatigue (r=0.613, p<0.001) and anxiety (r=0.687, p<0.001) in women and higher perceived stress (r=0.449, p=0.002) across all participants.

Conclusions The microstructural alterations in the PASC group are similar to those reported in stress-related disorders and might be exacerbated by stress.

Light-Activatable Ethanol Injection for the Treatment of Locally Unresectable Tumors

Chen-Hua Ma, Jeffrey Yang, Jenna L. Mueller, Huang-Chiao Huang
Fischell Department of Bioengineering, University of Maryland, College Park, MD 20742

Background: Percutaneous ethanol injection, which involves direct injection of ethanol into tumors to induce necrosis, is an inexpensive ablative treatment option for patients with localized tumor nodules. It has also been combined with other local ablative therapies to produce synergistic effects and treat larger tumors up to 7 cm in diameter. However, its efficacy is limited due to poor distribution and leakage of therapy from the tumor, often causing normal tissue toxicity. To improve the treatment efficacy of intratumoral ethanol injection, our team has developed a light-activatable ethanol injection (LEI) formulation that contains ethanol, a cellulose derivative, and a photosensitizer. A cellulose derivative was selected because of its ability to form a cohesive local gel when injected into tissue, reducing leakage of both ethanol and the photosensitizer from the tumor[1]. Photosensitizers are used for photodynamic therapy, which involves their absorbing visible light to generate reactive oxygen species and induce cell death. The activated photosensitizers can also emit fluorescence signals, enabling visualization of their local distribution via optical imaging[2]. While photodynamic therapy is clinically promising for treating inoperable cancers, its efficacy could be limited due to photosensitizer self-quenching after an intratumoral injection.

Objective: Our goal is to improve photosensitizer retention and evaluate if the photophysical and photochemical properties are maintained in our new formulation.

Methods: To study the distribution of our LEI formulation in tissues, cellulose derivative, ethanol, and photosensitizers were mixed at different volume ratios and injected into tissue mimicking phantoms and excised swine livers to form a uniform depot. Using our customized widefield fluorescence microscope, the photosensitizer fluorescence signal can be imaged to reveal the distribution volume of the depot in sectioned phantoms or tissues. To test if our LEI formulation can be activated by red light to produce singlet oxygen in tissues, SOSG™ (singlet oxygen sensor green) were added into LEI formulation prior to injection. A 690 nm CW laser was used to irradiate the depot at different radiant exposures. After light irradiation, the SOSG signal (ex/em. 505/525 nm) was detected. The above fluorescence imaging and additional flow cytometry studies will allow us to test if ethanol helps de-quench photosensitizers and subsequently improve the distribution of photosensitizers in tissue.

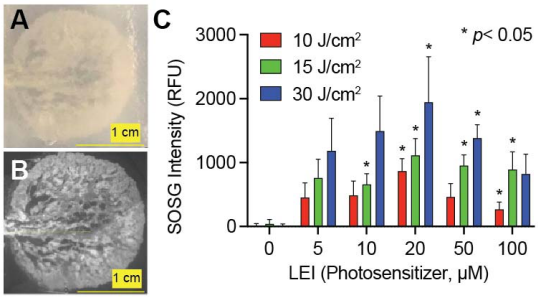

Figure 1. (A) Digital and **(B)** fluorescence images of the LEI formulation cross-section distribution in 1% agarose phantom. **(C)** Light (690 nm, 50mW/cm^2) activation of the LEI formulation produces singlet oxygen detected by SOSG™.

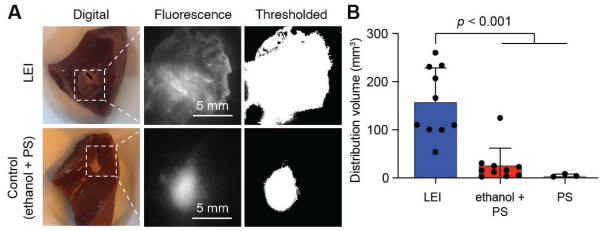

Figure 2. (A) Representative fluorescence and binary images of LEI formulation injections and a control (photosensitizer (PS)-ethanol) in swine liver tissues (images are cross-sections through the depot). **(B)** Average distribution volumes show that LEI significantly increases the depot volume in tissues, compared to controls (PS-ethanol; PS alone).

Results: We showed that LEI can be injected into tissue mimicking phantoms to form a uniform depot of ~2 cm in diameter (Fig. 1A). The photosensitizer fluorescence signal can be imaged to reveal the distribution volume of LEI in the phantoms (Fig. 1B). Light activation of LEI resulted in singlet oxygen generation in an optical dose- and photosensitizer concentration-dependent manner (Fig. 1C). Similar to the phantom study, fluorescence imaging of photosensitizers can be used to visualize the LEI depot volume in swine liver tissues (Fig. 2A). We found that LEI increased depot volume by 6-fold (Fig. 2B), compared to that of the monotherapies.

Conclusions: LEI distribution into tissue mimicking phantoms and swine liver tissues can be monitored by imaging the photosensitizer fluorescence signal. The cellulose derivative is a key component of our formulation that could increase the depot distribution area. Future studies will investigate the efficacy and safety of LEI in *in vivo* tumor models.

References: [1] R. Morhard, C. Nief, C. Barrero Castedo, F. Hu, M. Madonna, J. L. Mueller, M. W. Dewhirst, D. F. Katz and N. Ramanujam, Sci Rep 2017, 7, 8750.
[2] B. Gaitan, C. T. Inglut, Y. Liu, Y. Chen and H. C. Huang, J Biomed Opt 2020, 25.

TITLE: Advancing Laser Interstitial Thermal Therapy for Glioblastoma Using Targeted Gold Nanoparticles

AUTHORS

Sumiao Pang PhD student Fischell Department of Bioengineering University of Maryland College Park sumiao@umd.edu
Anthony J. Kim, PhD Co-Director of Translational Therapeutics Research Group, Adjunct Associate Professor of Bioengineering (College Park) and Pharmaceutical Sciences (School of Pharmacy) University of Maryland School of Medicine AKim@som.umaryland.edu
Jeffrey A. Winkles, PhD Professor in Surgery, Neurosurgery, and Physiology Departments University of Maryland School of Medicine JWinkles@som.umaryland.edu
Graeme F. Woodworth, MD Professor in Neurosurgery, Diagnostic Radiology Nuclear Medicine, Anatomy & Neurobiology; Director of the Brain Tumor Treatment & Research Center; Chair, Department of Neurosurgery University of Maryland School of Medicine GWoodworth@som.umaryland.edu
Huang-Chiao Huang, PhD Assistant Professor Fischell Department of Bioengineering University of Maryland College Park hchuang@umd.edu

BACKGROUND Glioblastoma (GBM) is categorized by the World Health Organization as one of the most malignant and invasive types of brain cancer that currently has a 5-year survival rate of less than 10% [1-4]. Tumor recurrence is nearly universal due to its invasive characteristics, limited delivery of therapeutic agents, and persistent drug resistance[3,4]. The current standard treatment options are maximal safe resection followed by combined chemo-radiotherapy and adjuvant chemotherapy which result in a median patient overall survival [OS] of ~15 months [5, 6]. Significant developments in image-guided technologies that combine magnetic resonance imaging (MRI) and MR thermometry with laser interstitial thermal therapy (LITT) have recently been FDA approved (Visualase® and Neuroblate®) and shown promise in treating GBM patients. Based on clinical trials utilizing LITT for GBM tumor ablation, this new approach can provide a minimally invasive treatment option to GBM patients within the standard stereotactic biopsy surgical workflow. LITT has been shown to improve the median overall survival by an additional 10.2 months [7]. However, due to LITT's use of high laser power (up to 15 W), lack of cellular selectivity, and GBM cells' invasive nature, injury to adjacent brain tissues during and after LITT is a major obstacle to overcome. Gold nanoparticle (AuNP)-enhanced photothermal treatments can increase thermal conductance and capacitance within the tumor and reduce heat transfer to surrounding normal tissues [8-11]. Additionally, the tumor necrosis factor receptor superfamily (TNFRSF) member fibroblast growth factor-inducible 14 (Fn14) is an attractive receptor to target. High expression of Fn14 have been reported in 70-85% of GBM tumors while typically not expressed in healthy brain tissue [12-14].

OBJECTIVE The objective is to improve the therapeutic index of LITT by using controlled intratumoral delivery of a novel Fn14-targeted AuNP formulation which may enable (i) image-guided treatment, (ii) GBM cell selectivity, and (iii) controlled tumor heating; thus, reducing side effects on surrounding healthy brain tissues.

METHODS

Fn14 antibody (ITEM4)-coated AuNP synthesis. Gold nanorods PEGylated with 1 kDa PEG-COOH were purchased from nanoComposix. Conjugation of ITEM4 was accomplished using EDC-NHS chemistry for 4 hours at room temperature.

Phantom infused AuNPs. Phantoms were made using agarose powder (0.6%). Once all agarose powder was dissolved, temperature was maintained at ≤ 40ºC to infuse various AuNP formulations and concentrations.

RESULTS

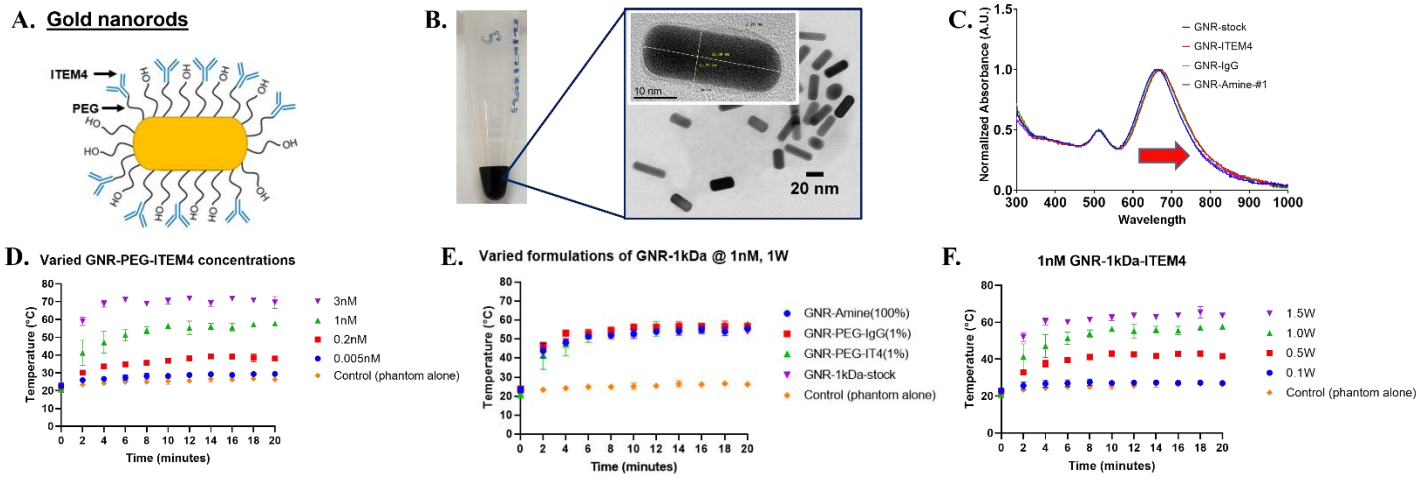

Figure 1. Characterization of Fn14-targeted AuNPs conjugated with ITEM4 antibodies. (A) Schematic of Fn14-directed AuNP, (B) TEM images, and (C) UV-VIS spectrum. Photothermal results of phantom infused AuNPs with (A) varied gold nanorod concentrations, (B) varied gold nanorod formulations, and (C) varied laser powers.

CONCLUSION

Fn14 antibody (ITEM4)-coated AuNPs are well characterized using TEM imaging and UV-VIS spectrum which shows that our particles are stable post conjugation. Furthermore, photothermal results from phantom infused AuNPs demonstrate our formulation can be light activated (i) to achieve a maximum temperature of 60ºC, (ii) with as low as 0.5 W laser power, and (iii) with as low as 0.2 nM concentration. Future work will involve *in vitro* and *in vivo* studies to understand cellular targeting and treatment effects using image-guided Fn14-directed AuNP assisted LITT technology.

REFERENCES

[1] D. T. Di Carlo, F. Cagnazzo, N. Benedetto, R. Morganti, and P. Perrini, "Multiple high-grade gliomas: epidemiology, management, and outcome. A systematic review and meta-analysis," (in eng), *Neurosurg Rev,* vol. 42, no. 2, pp. 263-275, Jun 2019, doi: 10.1007/s10143-017-0928-7.

[2] L. Marenco-Hillembrand *et al.*, "Trends in glioblastoma: outcomes over time and type of intervention: a systematic evidence based analysis," (in eng), *J Neurooncol,* vol. 147, no. 2, pp. 297-307, Apr 2020, doi: 10.1007/s11060-020-03451-6.

[3] Q. T. Ostrom, G. Cioffi, K. Waite, C. Kruchko, and J. S. Barnholtz-Sloan, "CBTRUS Statistical Report: Primary Brain and Other Central Nervous System Tumors Diagnosed in the United States in 2014-2018," (in eng), *Neuro Oncol,* vol. 23, no. 12 Suppl 2, pp. iii1-iii105, 10 05 2021, doi: 10.1093/neuonc/noab200.

[4] A. L. Stensjøen, O. Solheim, K. A. Kvistad, A. K. Håberg, Ø. Salvesen, and E. M. Berntsen, "Growth dynamics of untreated glioblastomas in vivo," (in eng), *Neuro Oncol,* vol. 17, no. 10, pp. 1402-11, Oct 2015, doi: 10.1093/neuonc/nov029.

[5] J. N. Cantrell *et al.*, "Progress Toward Long-Term Survivors of Glioblastoma," (in eng), *Mayo Clin Proc,* vol. 94, no. 7, pp. 1278-1286, 07 2019, doi: 10.1016/j.mayocp.2018.11.031.

[6] P. Zhang, Q. Xia, L. Liu, S. Li, and L. Dong, "Current Opinion on Molecular Characterization for GBM Classification in Guiding Clinical Diagnosis, Prognosis, and Therapy," (in eng), *Front Mol Biosci,* vol. 7, p. 562798, 2020, doi: 10.3389/fmolb.2020.562798.

[7] N. Montemurro, Y. Anania, F. Cagnazzo, and P. Perrini, "Survival outcomes in patients with recurrent glioblastoma treated with Laser Interstitial Thermal Therapy (LITT): A systematic review," (in eng), *Clin Neurol Neurosurg,* vol. 195, p. 105942, 08 2020, doi: 10.1016/j.clineuro.2020.105942.

[8] E. B. Dickerson *et al.*, "Gold nanorod assisted near-infrared plasmonic photothermal therapy (PPTT) of squamous cell carcinoma in mice," (in eng), *Cancer Lett,* vol. 269, no. 1, pp. 57-66, Sep 2008, doi: 10.1016/j.canlet.2008.04.026.

[9] Z. Qin and J. C. Bischof, "Thermophysical and biological responses of gold nanoparticle laser heating," (in eng), *Chem Soc Rev,* vol. 41, no. 3, pp. 1191-217, Feb 2012, doi: 10.1039/c1cs15184c.

[10] H. C. Huang, S. Barua, D. B. Kay, and K. Rege, "Simultaneous enhancement of photothermal stability and gene delivery efficacy of gold nanorods using polyelectrolytes," (in eng), *ACS Nano,* vol. 3, no. 10, pp. 2941-52, Oct 2009, doi: 10.1021/nn900947a.

[11] H. C. Huang, K. Rege, and J. J. Heys, "Spatiotemporal temperature distribution and cancer cell death in response to extracellular hyperthermia induced by gold nanorods," (in eng), *ACS Nano,* vol. 4, no. 5, pp. 2892-900, May 2010, doi: 10.1021/nn901884d.

[12] J. G. Perez *et al.*, "The TWEAK receptor Fn14 is a potential cell surface portal for targeted delivery of glioblastoma therapeutics," (in eng), *Oncogene,* vol. 35, no. 17, pp. 2145-55, 04 28 2016, doi: 10.1038/onc.2015.310.

[13] N. L. Tran *et al.*, "The human Fn14 receptor gene is up-regulated in migrating glioma cells in vitro and overexpressed in advanced glial tumors," (in eng), *Am J Pathol,* vol. 162, no. 4, pp. 1313-21, Apr 2003, doi: 10.1016/S0002-9440(10)63927-2.

[14] D. S. Hersh *et al.*, "The TNF receptor family member Fn14 is highly expressed in recurrent glioblastoma and in GBM patient-derived xenografts with acquired temozolomide resistance," (in eng), *Neuro Oncol,* vol. 20, no. 10, pp. 1321-1330, 09 03 2018, doi: 10.1093/neuonc/noy063.

A miniaturized multicontrast microscope for neurovascular imaging in freely moving animals

Janaka Senarathna, PhD[1] and Arvind P. Pathak, PhD[1]
[1]Russel H. Morgan Department of Radiology and Radiological Science,
The Johns Hopkins School of Medicine, Baltimore, MD, USA, 21205

Background: Imaging multiple neurophysiological variables in animals permits comprehensively assessing their brain function during healthy and disease conditions. However, instruments that can image multiple variables do so by acquiring images with multiple contrasts, and therefore require a substantially larger number of components than single-variable imaging systems, making them large and stationary. Their stationary nature requires animals to be anesthetized and/or immobilized, precluding the correlation of behavior with brain activity. Anesthesia can also alter the brain function being investigated. Moreover, such systems typically require customized designs, expert operators and may be expensive, significantly limiting their affordability.

Objective: To address these drawbacks, we aimed to create a low-cost, easy-to-operate miniaturized microscope that can investigate brain function with three optical contrasts: fluorescence (FL), intrinsic optical signals (IOS) and laser speckle contrast (LSC).

Methods: We used two surface-mount light emitting diodes (LEDs) at center wavelengths of 453 nm and 530 nm for green FL excitation and IOS imaging, respectively. Here, the FL excitation wavelength was sufficiently left-shifted as no excitation filter was used due to space limitations. A 510 nm longpass filter was placed in the imaging path to permit illumination from other light sources to pass while preventing the excitation light form reaching the image sensor. Moreover, the 530 nm wavelength was chosen as it is an isosbestic point in the oxy- and deoxy-hemoglobin spectra. A 680 nm vertical cavity surface emitting laser (VCSEL) diode was used to provide illumination for LSC imaging. We then used a single aspheric lens with a focal length of 4.6 mm to collect light via a 1.6 mm diameter aperture and focus it only a complementary metal-oxide semiconductor (CMOS) image sensor. Most of the microscope housing was designed using a computed aided design (CAD) software, and 3D printed to minimize device weight. We also developed a graphical user interface (GUI) to control imaging parameters and acquisition.

Results: Our microscope weighted 3 g after the application of a strain relief mechanism, and was able to image in freely behaving animals a field of view (FoV) of 3x3 mm^2 at 5 µm resolution and 10 frames per second. **Figs. 1a** and **b** show schematics of the bottom and side views of our design. The microscope attaches to a 3D printed head-mount affixed atop a surgically prepared cranial window on the animal's head. It's FL channel enabled imaging neuronal activity via calcium-bound GCaMP fluorescence. The IOS and LSC channels enabled imaging microvascular structures and vasodilations/vasoconstrictions, i.e., changes to cerebral blood volume (CBV), and cerebral blood flow (CBF), respectively. First, we compared images acquired via the miniaturized microscope for each channel with those acquired from a standard benchtop-based optical imaging system, and demonstrated a high degree of correlation. We then used it to interrogate neurovascular coupling in an awake mouse auditory cortex in relation to a sound stimulus at 4 kHz (**Fig. 1c**). The stimulus was presented for 300 ms at 3 seconds during a 10-second epoch. **Figs. 1d-f**, illustrate time-lapse images of neuronal activity, CBV and CBF averaged over 25 trials, and showcase both the spatial and temporal mismatch between the functional activations of each neurophysiological variable.

Conclusion: Our microscope is an excellent tool to interrogate neurovascular coupling in freely moving animals. We are currently working on the next generation of our microscope and looking for strategic partners to enable exciting discoveries in both basic neuroscience and preclinical research.

Figure 1: Investigating neurovascular coupling with a miniaturized multicontrast microscope. (**a - b**) Schematic showing the bottom and side view of the microscope assembly. (**c**) The experimental setup. (**d - f**) time lapse images for the first 4 seconds of the experiment showing neuronal activity, CBV and CBF, respectively. Scale bars indicate 5 mm and 500 µm in (**a**, **b**) and (**d-f**), respectively. Images reproduced with permission from: https://www.nature.com/articles/s41467-018-07926-z.

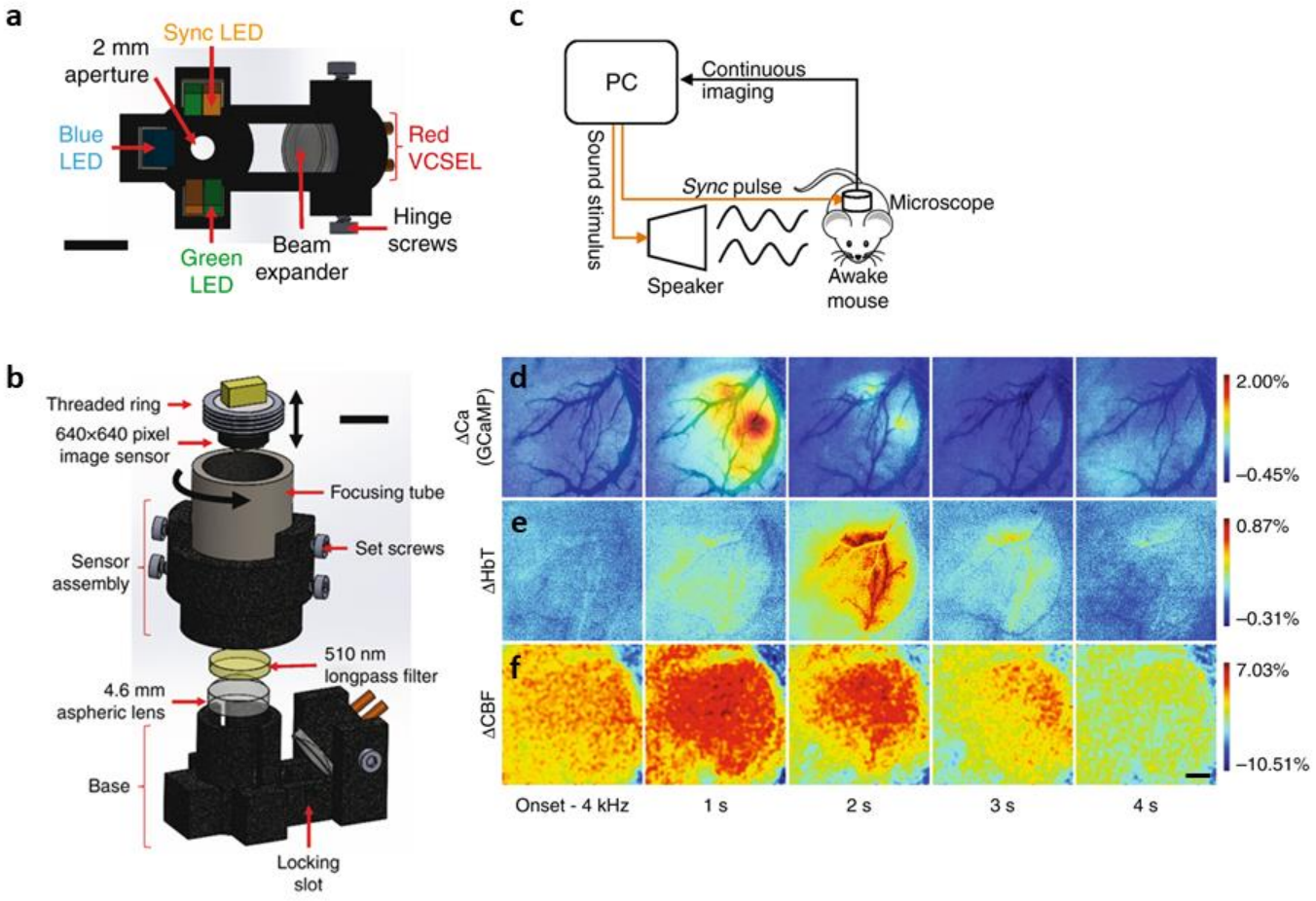

Figure 1: Investigating neurovascular coupling with a miniaturized multicontrast microscope.

Significance of ^{68}Ga-DOTATOC as a marker for neuroendocrine tumors (NETs)

[1]Shrestha BB MBBS, [1]Shah RP MD, [1]Singh SB MBBS, [1]Valluru S MBBS, [1]Raynor WY MD
Department of Radiology, University of Pennsylvania

Background: Neuroendocrine tumors (NETs) are a type of slow-growing neoplasm that originate from cells found primarily in the lungs, the gastroenteropancreatic system, thyroid, adrenal and pituitary glands. The limitations of traditional morphological imaging, and the delay in the diagnosis of neuroendocrine primary tumors and metastases raises the importance of PET imaging with Ga-DOTATOC. ^{68}Ga-DOTATOC has better sensitivity, faster clearance, reduced radiation exposure, and limited toxicity. ^{68}Ga-DOTATOC PET/CT is the gold standard for diagnosis and staging of most NETs. However, the potential of ^{68}Ga-DOTATOC as a potential theranostic is yet to be explored. In addition to being a favorable prognostic indicator, ^{68}Ga-DOTATOC uptake is a good prognostic index of response to PRRT Peptide Receptor Radionuclide Therapy.

Objective: To explore the usefulness of ^{68}Ga-DOTATOC in management of NETs. To describe advantages, disadvantages, and challenges for its routine clinical use in the diagnosis and treatment of NETs.

Methods: Highly cited articles on ^{68}Ga-DOTATOC published in the last 5 years in PubMed and Google Scholar were searched using the keywords "^{68}Ga-DOTATOC", "neuroendocrine tumors (NETs)" and "theranostics". They were reviewed and analyzed to collect important information about their utility, benefits, and drawbacks. The information was recorded in an excel sheet before constructing a complete abstract.

Results: NETs are difficult to identify and diagnose due to vague symptomatology, including bloating and weight loss. Patients with NETs around the world have reported concerns about their care, including diagnostic delays and a lack of appropriate imaging studies for NETs. The majority of NETs express Somatostatin Receptors (SSTR), which can be used as radionuclide imaging and targets. The advent of ^{68}Ga-labeled somatostatin (SST) analogues for imaging with PET/CT (such as ^{68}Ga-DOTA-TOC, ^{68}Ga-DOTA-TATE, and ^{68}Ga-DOTA-NOC) has resulted in a promising alternative for NET diagnosis and staging. Due to significant improvement in investigation time (90 minutes vs 24 hours) and decreased radiation dose (3 mSv vs 9 mSv), ^{68}Ga-DOTATOC is proved to be superior to ^{111}In-Octreotide SPECT/CT in NETs diagnostics. In addition, the SSTR PET scan can be done one hour after the radiopharmaceutical has been injected, which is more convenient for the patients. ^{68}Ga-SSTR PET/CT has a sensitivity of 88–93% and a specificity of 88–95% for most NETs. In comparison to morphological imaging modalities, SSTR PET/CT exhibited superior accuracy for the detection of NET lesions. In addition to being a favorable prognostic indicator, 68Ga-DOTA-conjugate uptake is a good prognostic index of response to PRRT Peptide Receptor Radionuclide Therapy. Furthermore, ^{68}Ga-DOTATOC appears to be effective in examining individuals with relevant symptoms and laboratory findings, however it performs poorly and has a low yield in this situation. Also, NETs of unknown origin (sensitivity 68 %, specificity 52 %) and benign insulinomas, which are usually small and have low SSTR2 expression, result in poorer diagnostic accuracy by SSTR PET/CT. It is useful in determining the location of an unknown primary tumor in NET patients who have metastatic NET but no known primary tumor. The sensitivity of 68Ga-DOTA-TOC for detecting atypical carcinoid tumors is significantly lower than for typical carcinoid tumors. Until now, the importance of imaging technologies in assessing therapy response has been a matter of discussion.

Conclusions: In conclusion, ^{68}Ga-DOTATOC PET/CT is the gold standard for diagnosis and staging of most NETs. ^{68}Ga-DOTATOC has been found to outperform structural imaging in the theranostics of NETs. Future studies are warranted to determine the appropriate indications for its routine clinical use. However, there is not enough research to recommend ^{68}Ga-DOTATOC PET as part of treatment response assessment and follow-up.

BOLD fMRI-Based Brain Perfusion Prediction Using Deep Dilated Wide Activation Networks

Yiran Li[1], Danfeng Xie, PhD[1], Ze Wang, PhD[1]

1. Department of Diagnostic Radiology and Nuclear Medicine, University of Maryland School of Medicine, Baltimore, MD, USA

Background

Arterial spin labeling (ASL) perfusion MRI quantifies regional cerebral blood flow (CBF) and subsequently provides a marker for assessing regional brain functions. However, ASL MRI is not available in many research sites. By contrast, the blood-oxygen-level-dependent (BOLD) fMRI has been a standard neuroimaging research tool and is included in almost any large size fMRI project. Since CBF provides several advantages over BOLD fMRI for assessing brain function, including better localization capability, insensitivity to low-frequency drift, offering quantitative measurement etc., it is of great scientific interest to develop a method to predict the missing ASL CBF from the existing BOLD fMRI. Built upon BOLD fMRI, the method would compensate some of the existing drawbacks of ASL MRI such as the low signal-to-noise-ratio, low temporal resolution. The purpose of this study was to assess a deep learning (DL)-based BOLD predicting ASL model.

Objective

The objective of this study was to develop a technique that can combine the advantages of BOLD fMRI and ASL MRI, i.e., to quantify cerebral blood flow (CBF) like ASL MRI but with high SNR and temporal resolution as in BOLD fMRI. We pursued this goal using a new deep learning-based algorithm to extract CBF directly from BOLD fMRI. Using a relatively large dataset containing dual-echo ASL [1] and BOLD images, we built a wide residual learning based convolutional neural network to predict CBF from BOLD fMRI.

Methods

The DL-based model is called Dilated Wide Activation Networks. The two-path DilatedNet [2] were used to extract both local and global contextual features. The wide activation residual blocks were adapted to expand data features and pass more information through the network [3]. Inspired by [4], even we do not have gold standard CBF maps as the training references, using the low SNR ASL CBF can still produce good prediction.

Results

As compared to the genuine mean CBF map from the acquired ASL MRI, the CBF map produced by the proposed model showed substantially improved quality in terms of suppressed noise and better perfusion contrast between tissues.

Conclusion

This study represents the first effort to extract quantitative CBF from BOLD fMRI. The proposed model can provide CBF measurement with higher SNR, higher temporal resolution, both inherited from BOLD fMRI (higher SNR is also contributed by DL denoising). For existing dataset without ASL MRI acquired, this provides a unique opportunity to generate a new functional imaging modality.

1. Shin, D.D., Liu, T.T., Wong, E.C., Shankaranarayanan, A., Jung, Y.: Pseudocontinuous arterial spin labeling with optimized tagging efficiency. Magn. Reson. Med. 68, 1135–1144 (2012).
2. Kim, K.H., Choi, S.H., Park, S.-H.: Improving arterial spin labeling by using deep learning. Radiology. 287, 658–666 (2018).
3. Yu, J., Fan, Y., Yang, J., Xu, N., Wang, Z., Wang, X., Huang, T.: Wide activation for efficient and accurate image super-resolution. arXiv Prepr. arXiv1808.08718. (2018).
4. Lehtinen, J., Munkberg, J., Hasselgren, J., Laine, S., Karras, T., Aittala, M., Aila, T.: Noise2Noise: Learning image restoration without clean data. arXiv Prepr. arXiv1803.04189. (2018).

The usefulness of Fibroblast activation protein inhibitor (FAPI) in the detection of various malignancies

1,2 Rajendra Shah MBBS, 1,3 Shashi Singh, 1,3 Bimash B Shrestha, 1,4 Sahith Valluru
1 University of Pennsylvania, PA; 2 Nuvance health, NY; 3 KIST Medical College, Nepal; 4 Narayana Medical College, India

Background: Currently,18F-FDG is the most commonly used radiotracer. However, in the context of stromal tumors, new radiotracers with higher sensitivity and lower tumor to background ratios are being investigated. One such radiotracer is Fibroblast activation protein inhibitor (FAPI). Fibroblast activation protein (FAP) is a 760-amino-acid type II transmembrane glycoprotein that belongs to the serine protease family. It is found in stromal fibroblasts in more than 90% of epithelial malignancies and malignant cells in glioblastoma, breast, colorectal, cervical, and oral squamous cell carcinomas. In cancer patients, overexpression of FAP is associated with increased local tumor motility and invasiveness, lower survival, and a bad prognosis. FAPI has demonstrated promising results in diagnosing and treating certain solid cancers. However, there is a scarcity of research comparing FAPI with FDG PET/CT in terms of tracer uptake, tumor-to-background ratio, detection of primary and metastatic tumors, and their implications for patient care. Moreover, the theranostic effect of FAPI has not been assessed in detail.

Objective: To compare the usefulness of FAPI-PET/CT over FDG-PET/CT in various malignancies for uptake of tracer, tumor-to-background ratio, and detection of primary and metastatic tumors.

Methods: We searched databases like PubMed and Google Scholar to compile the existing articles describing the data generated by FAPI PET/CT and compared the results to FDG PET/CT in various primary and metastatic tumors. We reviewed systemic reviews, meta-analyses, scientific articles, literature reviews, letters to the editor, and case reports related to the use of FAPI and FDG in the diagnosis and evaluation of tumors. FAPI-PET/CT and 18F-FDG PET/CT were evaluated based on differences in four main categories: tracer uptake, tumor-to-background ratios, detection of primary tumors, and detection of secondary metastatic tumors.

Results: Most studies have been performed in a mixed population of different cancers, but recently more studies for specific cancers have been published. A mixed type of results has been obtained while comparing these two radiotracers. FAPI PET/CT was found to have higher specificity, tumor to background ratio, tracer uptake, and detection of primary and secondary metastatic tumors compared to 18F-FAPI PET/CT. Komek et al. (2021) found significantly higher maximum standardized uptake values (SUV_{max}) for ^{68}Ga-FAPI compared to ^{18}F-FDG in primary breast tumors and lymph node, lung, and bone metastases. In a systematic review by Treglia et al. (2021), all included studies demonstrated lower uptake of radiolabeled FAPI in normal brain, liver, and oral mucosa compared to ^{18}F-FDG. This finding was reiterated by Syed et al. (2021), in which ^{68}Ga-FAPI demonstrated higher uptake in tumors but lower background uptake in healthy tissues. Because of its lower expression in normal organs, FAP is also a promising target for theranostics. Since FDG physiologically accumulates in the ovary, there is high tumor to background contrast, increasing the diagnostic difficulty for ovarian diseases. However, there is no physiological accumulation of FAPI in the ovary, increasing its importance in the early and accurate diagnosis of ovarian cancer. The relatively short half-life constrains the [68Ga] Ga-FAPI, whereas 18F-labeled FAPI has a relatively longer half-life making it more useful.

Conclusions: FAPI PET/CT has shown promising results compared to FDG PET/CT in evaluating certain types of solid cancers, but further research needs to be conducted to determine its clinical usefulness. FAPI's potential as a theranostic tool should also be investigated in detail.

Role of [18 F]-SMBT1 in the Alzheimer's disease

1,2 Rajendra Shah MBBS, 1,3 Shashi Singh, 1,3 Bimash B Shrestha,
1 University of Pennsylvania, PA; 2 Nuvance health, NY; 3 KIST Medical College, Nepal;

Background

Alzheimer's disease is the most common cause of dementia and one of the leading sources of morbidity and mortality in the aging population. Alzheimer's disease is neuropathologically characterized by diffuse and neuritic plaques, marked by extracellular amyloid-beta deposition, and neurofibrillary tangles, comprised of the intracellular accumulation of hyperphosphorylated tau (p-tau) protein. Reactive astrocytes and activated microglia are found to have a major role in contributing to neurodegeneration in Alzheimer's disease so PET imaging of reactive astrocytes will give a better understanding of the underlying illness process, as well as helps monitoring of the glial response to disease-modifying therapies. The gold standard marker of reactive astrocytes is intermediate filament such as GFAP. MAO-B (monoamine oxidase-B and I2BS (imidazoline2 binding sites) are surrogate targets of reactive astrogliosis. There are many radiotracers being studied for Alzheimer's disease which includes [11C] DED, [11C]SL25.1188, [11C] BU99008, [18F] THK-5351 and [18F]-SMBT1. [18F] - SMBT1 is a selective and reversible MAO-B radiotracer. [18F]-SMBT1 is one of the new radiotracers and there is very limited research related to [18F]-SBMT1 in Alzheimer's disease.

Objective

To discuss the role of [18F]-SBMT1 in Alzheimer's disease and compare it with other radiotracers being developed for Alzheimer's disease.

Methods

We searched the literature via PubMed and Google scholar to select the existing articles about radiotracers being used for Alzheimer's disease. We selected the papers that were highly cited. We will compare the pros and cons of different radiotracers using Alzheimer's disease.

Results

[18F]-SMBT1 was found to have a good pharmacokinetic profile, high MAO-B affinity, and decreased binding affinity to MAO-A and protein aggregates such as amyloid-beta and tau fibrils. Multiple in vivo studies suggested that reactive astrogliosis measured by MAO-B through [18F]-SMBT1 co-related to early Abeta accumulation. These studies were done on a wide range of human populations as well as on mice. Harada et al demonstrated that the MAO-B levels were upregulated in postmortem brain tissues of Alzheimer's disease, epilepsy, and Parkinsonian syndromes. [18F]-SMBT1 showed high uptake by the brain, rapid washout, and no radiolabeled metabolites in the brain of normal mice. The role of chirality of [18F]-SMBT1 in the imaging of Monoamine Oxidase-B warrants further investigation. Other radiotracers labeled with C-11 had limited widespread clinical medication. Fluorinated radiotracer is like [18F] THK-5351 are irreversible MAO-B inhibitors which limit their clinical use.

Conclusions

[18F]-SMBT1 has shown promising results for the imaging of reactive astrocytes in Alzheimer's disease but warrants further studies to establish its role. This radiotracer can be used in other neurodegenerative diseases well. The role of [18F]-SMBT1 can be established with further studies involving neurodegenerative disease.

Quantitative MRI of Electrostatic Molecular Binding Using the Water Proton Signal

Chongxue Bie[1,2,3], Yang Zhou[1,2,4], Peter C. M. van Zijl[1,2], Jiadi Xu[1,2], and Nirbhay N. Yadav[1,2]

[1] F.M. Kirby Research Center for Functional Brain Imaging, Kennedy Krieger Institute, Baltimore MD 21205 (USA) [2] The Russell H. Morgan Department of Radiology, The Johns Hopkins University School of Medicine, Baltimore, MD 21205 (USA) [3] Department of Information Science and Technology, Northwest University, Xi'an, Shaanxi 710127 (China) [4] Key Laboratory for Magnetic Resonance and Multimodality Imaging of Guangdong Province, Shenzhen Institute of Advanced Technology, Chinese Academy of Sciences, Shenzhen, Guangdong 518055 (China)

Background Electrostatic interactions play a fundamental role in mediating molecular interactions and are essential in many biochemical processes.[1] It was previously shown that transient molecular binding of natural ligands (no chemical modification) can be imaged using a saturation transfer (ST) MRI approach for enhancing sensitivity,[2] the so-called IMMOBILISE method. In the "IMMOBILISE" approach[2], the aliphatic protons of free ligands are first selectively labelled using a radio-frequency (RF) pulse. The binding-mediated saturation transfer effect is initiated by a ligand binding to an immobile receptor, which results in an intramolecular proton-proton cross-relaxation within the bound complex and finally to the water solvent via chemical exchange.

Objective Here, we detail the mechanism of water signal enhancement through molecular binding by a four-pool model, and verify the model using a small-charged molecule with ionic resin. The model, based on the detection of the relayed nuclear Overhauser effect (rNOE) MRI signal, can be described by a set of modified Bloch equations,[3] resulting in the analytical solution: $rNOE = rNOE_{max} \cdot \frac{[L]}{[L]+K_D}$ (1) where $[L]$ is the concentration of free ligands, $rNOE_{max}$ is a constant that determines the maximum detected signal, K_D is the dissociation constant. The binding parameters of the system can be quantified using the analytical solution.

Methods Various concentrations (10, 20, 50, 100, and 200 mM) of arginine (Arg) were dissolved in phosphate-buffered saline (PBS), pH of 7.2 and mixed with ion-exchange media (with functional groups -COO-). The mixture was pH-adjusted and transferred to the imaging tube for MRI measurements. Experiments were performed on a 17.6 T MR scanner at 20°C, using a 4 s CW RF pulse for labelling ligand protons followed by a RARE MRI readout of the water signal.

Results The interaction between Arg and negatively charged ion-exchange resin are in **Figure 1**. The saturation transfer spectra show the detection of Arg aliphatic protons at -0.9, -1.6, and -2.0 ppm, demonstrating the rNOE-based magnetization transfer from Arg aliphatic protons to water (**Figure 1A, B**). To determine molecular binding affinities, the rNOE signals were measured as a function of free ligand concentration and the curves were fitted using Eq. 1 to estimate K_D, which was about 130 mM for Arg to the resin (**Figure 1C**). Additionally, the rNOE maps could be obtained and show that rNOEs from different protons are comparable, indicating that the fast cross-relaxation is not rate-limiting (**Figure 1D**).

Conclusion We demonstrated the quantitative imaging of ionic binding parameters using the IMMOBILISE approach. These parameters combined with the obtained sensitivity enhancement provides a path to possible *in vivo* studies of molecular binding using MRI.

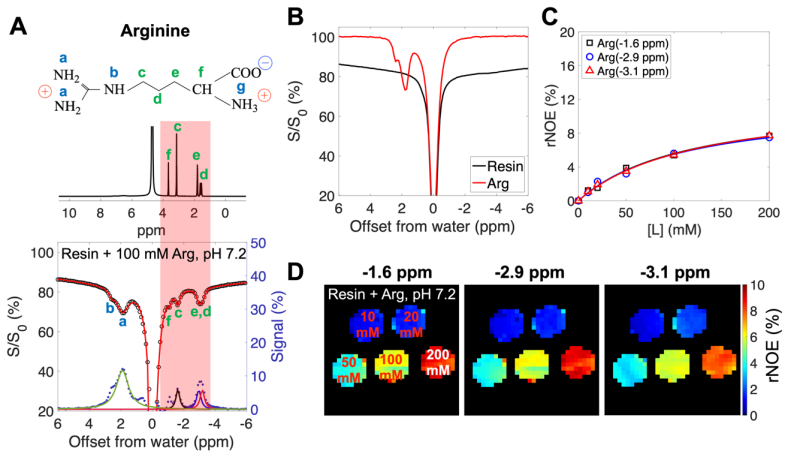

Figure 1. Z-spectroscopy of small-charged molecules mixed with ionic resin. (A-B) Chemical structure and ^{1}H NMR spectrum, individual Z-spectra of Arg and ionic resin solution, and Z-spectrum of resin with Arg (The extracted CEST and rNOE signals are also shown on the right vertical axis). (C) The measured IMMOBILISE signal intensities as a function of Arg concentration, together with a fit using Eq.1. (D) Maps of Arg rNOE signals at -1.6 ppm, -2.9 ppm, and -3.1 ppm. B_1 = 0.7 μT.

References 1. Nakamura H. Q Rev Biophys. 1996;29:1-90. 2. Yadav NN, et al., Sci Rep. 2017;7:10138. 3. Zhou Y, et al., ISMRM; 2021;0243.

Long-lasting effects of insufficient sleep on neurocognitive development in early adolescence

Fan Nils Yang, Ph.D.[1#]; Weizhen Xie, Ph.D.[2#]; Ze Wang, Ph.D.[1*]

[1]Department of Diagnostic Radiology and Nuclear Medicine, University of Maryland School of Medicine, Baltimore, MD, USA.
[2] National Institute of Neurological Disorders and Stroke, National Institutes of Health, Bethesda, MD, USA
# Contributed equally

Correspondence

*Ze Wang, Department of Diagnostic Radiology and Nuclear Medicine, University of Maryland School of Medicine, Baltimore, MD 21201, USA.

Email: Ze.Wang@som.umaryland.edu
Phone: +1-4107062797

Abstract

Background

Insufficient sleep is increasingly common in adolescents, however its long-term impact on the developing brain and behavior remains unknown.

Objective

To determine the impact of insufficient sleep on adolescents' behavior and brain over two years.

Methods

To estimate the long-term effects of insufficient sleep in adolescents, we leveraged large-scale data from the ongoing longitudinal Adolescent Brain Cognitive Development study, which involves 11,875 9-10-year-olds. Participants were separated into sufficient sleep (SS) versus insufficient sleep (IS) groups based on nine hours/day suggested by the American Academy of Sleep Medicine. Participants' behavioral problems, cognition, mental health, structural and rest-state functional brain measures were compared between SS and IS groups after controlling for 11 covariates (e.g., sex, socioeconomic status, puberty status) based on propensity score matching. Longitudinal mediation analyses were performed to examine neural correlates of behavioral changes induced by insufficient sleep.

Results

We identified 3021 matched SS-IS pairs at baseline and 749 matched pairs at 2-year follow-up, and observed reliable SS-IS differences in behavior and neural measures at both timepoints. The effect sizes of SS-IS differences at these two timepoints were significantly correlated (behavioral measures: r = 0.85, 95% CI: [0.73, 0.92], p < 1e-10; resting-state functional connectivity: r = 0.54 [0.45, 0.61], p < 1e-10; structural measures: r = 0.52 [0.40 to 0.61], p < 1e-

10), suggesting the temporal stability of compromised neurocognitive development induced by insufficient sleep. Furthermore, cortico-basal ganglia functional connections mediate the effects of sleep loss on depression and crystallized intelligence, and structural properties of the anterior temporal lobe mediate the impact of insufficient sleep on crystallized intelligence.

Conclusions

These results provide population-level evidence for the long-lasting impact of insufficient sleep on adolescents' mental health, cognition, and brain function and structure. These findings highlight the importance of early sleep intervention to improve adolescents' long-term developmental outcomes.

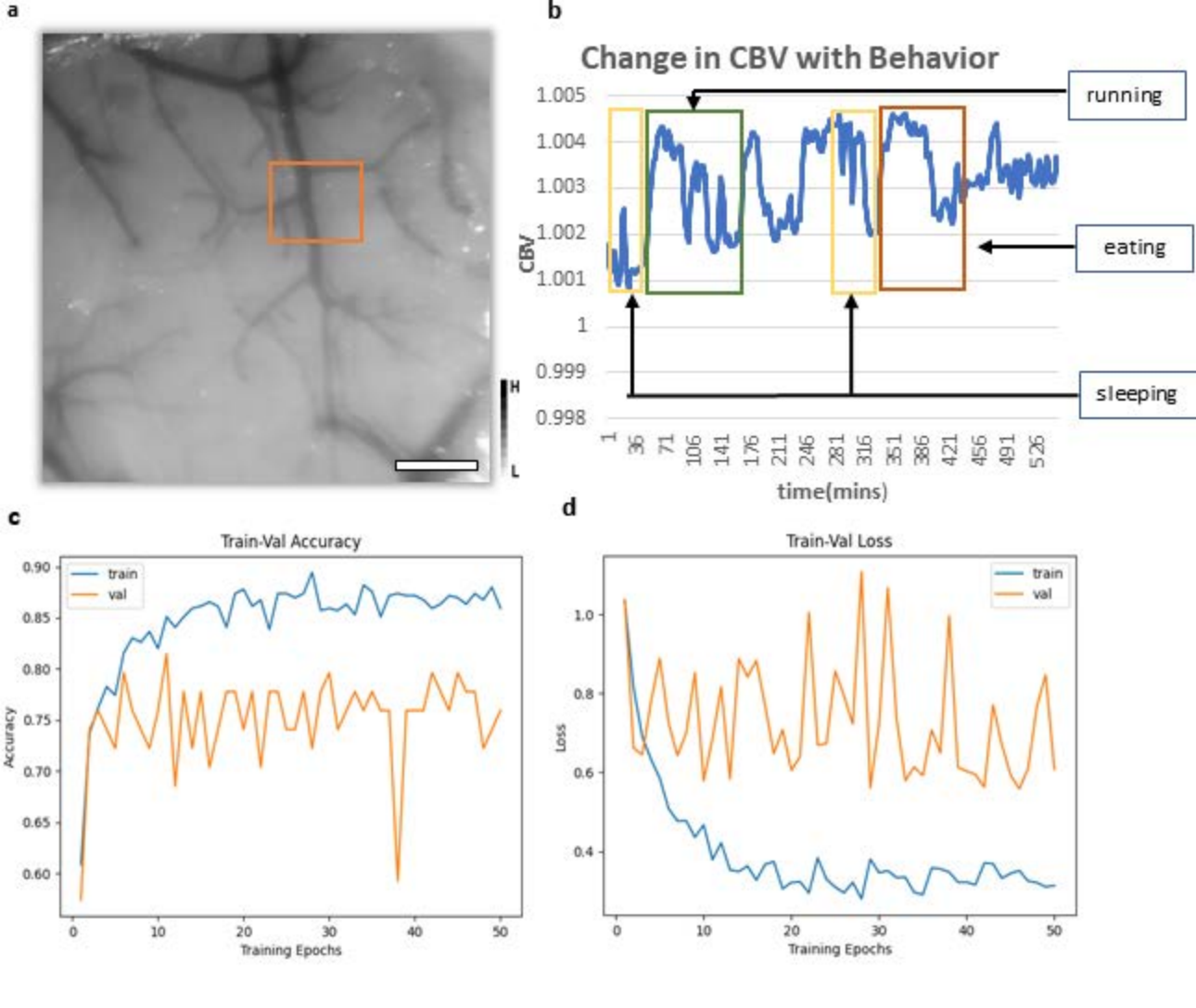

Fig. 1. The first 24 hours functional neuroimaging with time locked behaviors. a IOS map acquired under green light illumination showing HbT absorption scale bar indicates 500µm. b Time-series illustrating HbT (i.e., CBV) fluctuations corresponding to change in behaviors. c Training- validation accuracy of ResNet-LSTM d. Training-validation loss of ResNet-LSTM

PREDICTING ANIMAL BEHAVIOR FROM MULTICHANNEL NEUROIMAGING DATA WITH MACHINE LEARNING

Subhrajit Das[1], Janaka Senarathna[2], Darren Yang[4], Rishi Chandra[1], Amit Banerjee[3], Arvind Pathak[1,2,4]

[1]Depst. of Electrical and Computer Engineering. [2]Russell H. Morgan Department of Radiology and Radiological Science, Johns Hopkins University School of Medicine, Baltimore, MD 21205, USA [3]JHU Applied Physics Laboratory [4]Department of Biomedical Engineering, Johns Hopkins University School of Medicine, Baltimore, MD 21205, USA

Background: A fundamental goal of systems neuroscience is to understand the correlation between brain activity and behavior [1]. To achieve this, neuroscientists use miniaturized microscopes (or "miniscopes") that can be mounted atop an awake animal's head to acquire multichannel imaging data (e.g., brain activity, cerebral blood flow/CBF, cerebral blood volume/CBV), while another camera records the behavior [2]. Given the volume of multichannel imaging data as well as the complexity and heterogeneity of behaviors, it is challenging to predict one from the other. Although, several machine learning (ML) approaches have been proposed to address this need [1], many suffer from limited predictive accuracy and long processing times. To circumvent these drawbacks, we evaluated the ability of a state-of-the-art image sequence classifier called ResNet-LSTM, to predict animal behavior from multichannel neuroimaging data.

Objective: To develop an efficient video-level framework to accurately predict behavior from multi-channel neuroimaging data acquired using a miniscope on awake, freely behaving animals.

Methods: (i) *Data preparation*: Miniscopes [2] have allowed us to collect time-locked multichannel neuroimaging and behavioral data (**Fig. 1a, b**) via long-term (i.e., hours-days) animal experiments. We used behavior cloud software [3] to annotate behavioral "syllables" [1] within the behavioral video stream. Next, we labelled the time-locked neural activity image sequences with the corresponding behavior syllables. The final number of labelled image sequences in our dataset was 540. For each split, we used 484 and 56 image sequences for training and validation. (ii) *ML Models*: To classify images in a syllable, we used ResNet-LSTM. ResNet-LSTM is the combination of the Residual Network [5] model with a LSTM (Long Short-Term Memory). Residual models are widely used for the classification of isolated images, for example on ImageNet [4]. This model consist of convolution layers and contains residual connections every 2 layers. Residual connections are skip connections that skips two convolutional layers, which eases the training of these networks and enables them to be deeper, leading to better extraction of features and better accuracy. The LSTM is designed to model sequences and has been successfully applied in tasks such as speech recognition. The ResNet extracts the feature of our input neural activity image sequences. Pre-activations of the penultimate layer of ResNet were used as a feature vector and passed to a one-layer LSTM for modelling evolution via time steps. The number of neurons or units in the one layer of LSTM for extracting temporal features, was 1000. A linear layer after the LSTM calculated class scores for each image sequence. The model was trained during 50 epochs. An epoch represents the number of times the model (Resnet-LSTM) works through the entire training dataset of 484 labelled image sequences to classify them into their corresponding behaviors. The ResNet weights were pre-trained on ImageNet [4] and weights of LSTM components initialized randomly. Each training batch consisted of five syllables of 50 frames each, where frame resolution was resampled from 512×512 to 224×224 to reduce GPU memory usage.

Results: The training and validation accuracy are shown in **Fig. 1c**, while the training and validation losses are shown in **Fig. 1d**. We observed that our validation accuracy, which is how well the model classifies new image sequences non-existent in the training dataset, was 78.89%. This means that one syllable out of five was not classified properly. This is because one of the syllables did not have enough image sequences for the model to learn how to classify it.

Conclusion: We introduced a framework which uses one channel (i.e., fluorescence/neuronal) of our multichannel neuroimaging data to predict the associated behavior. We found that Resnet-LSTM successfully predicted the fluctuations in neuronal activity images during changes in behavior. Next, we will figure out if the prediction accuracy improves by using all three channels [2]. For our next experiments, we are planning to use 200 frames, which will successfully capture more neural activity in a single epoch, with a bi-directional LSTM to improve model performance.

References

1. Behave Net: nonlinear embedding and Bayesian neural decoding of behavioral videos. *33rd Conference on Neural Information Processing Systems (NeurIPS)*, Vancouver, Canada, 2019.
2. Senarathna J, Yu H, Deng C, Zou AL, Issa JB, Hadjiabadi DH, Gil S, Wang Q, Tyler BM, Thakor NV, Pathak AP. A miniature multi-contrast microscope for functional imaging in freely behaving animals. *Nat Commun* **10**: 99, 2019.
3. Behavior Cloud: https://behaviorcloud.com/
4. Krizhevsky A, Sutskever I, Hinton GE. ImageNet classification with deep convolutional neural networks. Advances in neural information processing systems. 2012;25.
5. He K, Zhang X, Ren S, Sun J. Deep residual learning for image recognition. In Proceedings of the IEEE conference on computer vision and pattern recognition 2016 (pp. 770-778).

In vivo MPI tracking of intra-arterially infused mesenchymal stem cells

A. Shakeri-Zadeh[1,2], S. Kuddannaya[1,2], A. Bibic[1,3], P Walczak[4], and J.W.M. Bulte[1,2,3*]

[1]The Russell H. Morgan Department of Radiology and Radiological Science, Division of MR Research, Baltimore, MD, USA; [2]Cellular Imaging Section and Vascular Biology Program, Institute for Cell Engineering, Baltimore, MD, USA; [3]F.M. Kirby Research Center for Functional Brain Imaging, Hugo W. Moser Institute, Kennedy Krieger Inc., Baltimore, MD, USA; [4]Department of Diagnostic Radiology and Nuclear Medicine, University of Maryland School of Medicine, Baltimore, MD, USA.
[*]Corresponding author, email: jwmbulte@mri.jhu.edu

Introduction: Several pre-clinical and clinical investigations have shown that stem cell therapy for the central nervous system is a potential strategy for treating a variety of diseases. Intra-arterial (IA) injection into the carotid artery is an appealing delivery route because it avoids initial uptake by systemic organs, allowing large numbers of cells to be delivered directly to the brain (1). Information on the effectiveness of this procedure and the amount of delivered cells is highly desirable for further optimization. In this study, we used magnetic particle imaging (MPI) combined with magnetic resonance imaging (MRI) to track human mesenchymal stem cells (hMSCs) labeled with superparamagnetic (SPIO) nanoparticles *in vivo* (2, 3).

Methods: Commercially available bone marrow-derived hMSCs (Rooster Bio, USA) were magnetically labeled with poly-L-lysine as transfection agent and the commercial SPIO formulation Resovist® (25 µg Fe/ml) in T-75 tissue culture flasks for 24 hours. Labeled cells were collected and prepared for IA injection into normal male Rag2 mice (n=3). Prussian blue staining and a Ferrozine-based spectrophotometric assay were used to assess intracellular iron uptake. Animal surgery and IA injection was performed as shown in **Figure 1A** and recently described elsewhere (4). Labeled cells were delivered into brain using 4 separate injections (30,000 cells each) with a time interval of 6 min between each injection. Whole body standard 2D MPI was performed before and after each injection. A final 2D MPI scan was obtained 30 min after the last injection. Animals were then sacrificed and the heads were imaged *ex vivo* with MRI using a 17.4T vertical bore Bruker Biospec scanner and then with MPI using a Magnetic Insight Momentum scanner. MR images were acquired using a FLASH sequence with TR=8.4 ms, TE=2.5 ms, NEX=16, FA=5 deg, resolution=0.1 mm, slice thickness= 18 mm, matrix size=150x300x180, and FOV=3x2x1.8 cm. Heads were scanned with MPI using the same FOV as MRI with 55 projections, 3D high resolution mode, and one scan per projection. A customized holder was 3D-printed for use with both MRI and MPI. Two fiducials containing 10,000 and 20,000 labeled hMSCs were placed within the MPI/MRI FOVs and used to register the MPI dataset with MRI using 3D slicer software.

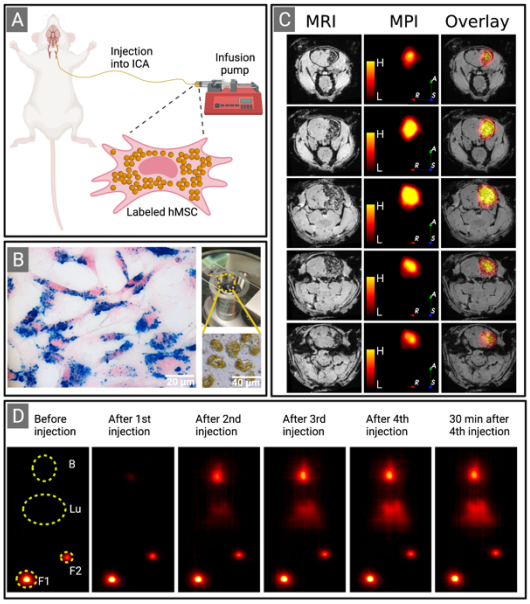

Figure 1. (A) Schematic outline of IA injection of Resovist-labeled hMSCs into the internal carotid artery (ICA). **(B)** Prussian blue staining of labeled hMSCs along with a microscopic image of live labeled cells before injection. **(C)** Five MPI/MRI slices from forebrain to midbrain (top to bottom) of a mouse injected with 120,000 labeled hMSCs. **(D)** Serial MPI images of a mouse before and after IA injection. In this panel, B, Lu, F1, and F2 stand for brain, lung, first fiducial (20,000 labeled hMSCs) and second fiducial (10,000 labeled hMSCs), respectively.

Results: Microscopic examination of a droplet of live cell suspension showed successful labeling of hMSC (**Figure 1B**, right bottom panel), which was later confirmed with Prussian blue staining. Figure 1B, left side, shows peri-nuclear accumulation of SPIOs in labeled hMSCs. An amount of 25 pg Fe per cell was measured by the Ferrozine assay. **Figure 1C** shows representative individual and overlay images of the *ex vivo* MRI and MPI datasets, where a unilateral distribution of labeled hMSCs at the side of IA injection can be seen. **Figure 1D** shows MP images of a mouse before and after IA injection, where hot spots in brain and lung as well as signal intensity alterations over time are present. When performing clinical stem cell transplantation studies, e.g., IA cell delivery to stroke patients, a main query is the number of cells that have arrived at the targeted tissue site and their spatial biodistribution. MPI/MRI hybrid imaging of magnetically labeled cells is a proper technique to address this issue. Aside from having quantitative and structural information together, the chief advantage of MPI/MRI hybrid imaging is the utilization of cold tracers (without radioactivity), allowing easy-to-interpret whole-body distribution studies. As shown in **Figure 1C**, our MPI/MRI data clearly show cerebral homing of labeled hMSCs after IA injection so that any region of interest can be quantified.

Conclusion: This successful example MPI application of *in vivo* tracking of hMSCs may encourage further use of this technique to probe the fate of therapeutic cells after transplantation.

References: 1) B. Rodríguez-Frutos, et al., Stem cell therapy and administration routes after stroke, *Translational stroke research*. **2016**; 7(5):378. **2)** J.W.M. Bulte, Superparamagnetic iron oxides as MPI tracers: A primer and review of early applications. *Advanced Drug Delivery Reviews*. **2019**; 138:293. **3)** J.W.M. Bulte, et al., Quantitative "hot-spot" imaging of transplanted stem cells using superparamagnetic tracers and magnetic particle imaging. *Tomography*. **2015**;1(2):91. **4)** C. Chu, et al., Hyperosmolar blood–brain barrier opening using intra-arterial injection of hyperosmotic mannitol in mice under real-time MRI guidance. *Nature Protocols*. **2022**; 17, 76.

The emerging role of [^{18}F]-FDG PET/CT in infectious and inflammatory disorders

[1]Singh SB MBBS, [1]Shrestha BB MBBS, [1]Shah RP MD, [1]Valluru S MBBS
Department of Radiology, University of Pennsylvania

Background: Although Henry N. Wagner Jr. mentioned 18-F fluoro-2-deoxyglucose (^{18}F-FDG) as the "tracer molecule of the 20th century", its importance is increasingly being understood and recognized in the 21st century. [^{18}F]-FDG is the most commonly used positron emission tomography (PET) tracer. It evaluates abnormal glucose metabolism and is now widely accepted in the diagnostic algorithms for most neoplasms. However, its use has expanded beyond diagnosing, staging, and monitoring neoplasms. One of its emerging use is imaging infection and inflammation. Nevertheless, due to a lack of studies with suitable gold standards, the clinical application of [^{18}F]-FDG to establish image interpretation criteria have yet to be explored.

Objectives: 1. To discuss the role of [^{18}F]-FDG in infection and inflammation. 2. To explore the potential uses of [^{18}F]-FDG for imaging infectious and inflammatory diseases in the clinical setting.

Methods: Highly cited articles on [^{18}F]-FDG PET/CT published in the last five years in PubMed and Google Scholar were searched using the keywords "[^{18}F]-FDG", "infection", and "inflammation." They were reviewed and analyzed to collect important information about their utility and ongoing uses. The data was recorded in an excel sheet before constructing a complete abstract.

Results: Infectious and inflammatory diseases can be assessed using [^{18}F]-FDG PET/CT given the avidity of inflammatory cells for glucose. It is a useful clinical tool for evaluating Pyrexia of unknown origin (PUO) and bacteremia of unknown origin (BUO) as it is able to detect infectious foci resulting in a shortened treatment period, reduced cost, and better prognosis. In AIDS patients presenting with neurologic symptoms, it can help distinguish between toxoplasmosis and central nervous system (CNS) lymphoma as FDG uptake is usually significant in CNS lymphoma but relatively modest or none in toxoplasmosis. Moreover, it effectively evaluates arterial inflammation in HIV; evaluates the efficacy of highly active antiretroviral therapy (HAART) based on nodal FDG uptake. It can also detect skeletal TB lesions, distinguish chronic TB spondylitis from acute pyogenic spondylitis, and differentiate osteomyelitis from aseptic post-operative or traumatic bone healing. It also has a higher diagnostic accuracy for detecting chronic vertebral osteomyelitis compared to a leukocyte scan. It is a valuable method for diagnosing large vessel vasculitis (LVV) like temporal arteritis, especially when temporal artery biopsy results are negative. Although [^{18}F]-FDG PET/CT detects early stages of LVV, its significance in smaller arteries is limited due to its inadequate spatial resolution. The FDG uptake in granulomatous cells that causes inflammation in sarcoidosis can be seen with [^{18}F]-FDG PET/CT. It is helpful for the classification and assessment of pulmonary and extrapulmonary sarcoidosis, and for measuring the efficacy of corticosteroids and infliximab in sarcoidosis. It helps in the diagnosis of suspected spinal infection (SI) in patients with elevated CRP and ESR, assessment of the extent of the SI, identification of complications, and evaluation of antibiotic response. The [^{18}F]-FDG PET/CT may detect undiagnosed COVID-19 cases in the early stages of infection when symptoms are nonspecific, and aid in initiating further workup, implementation of postexposure precautions, and recommendations. Ground glass opacifications (GGOs) with or without superimposed consolidation are seen on [^{18}F]-FDG PET/CT in a peripheral, basilar, and posterior predominant pattern, indicating increased metabolic activity in COVID-19. In addition to this, [^{18}F]-FDG PET/CT can also be used to investigate treatment responses in pulmonary fungal, viral, tuberculosis, and non-tuberculous mycobacterial infections, besides detecting occult infection in immunocompromised patients. [^{18}F]-FDG PET/CT is also helpful in cardiac diseases like endocarditis, diagnosis of foot complications, therapeutic monitoring, and follow-up in case of diabetic foot. However, it has less promising results in other pathologies, such as prosthetic joint infections. Still, it needs a lot of research to explore its uses in various infectious and inflammatory disorders.

Conclusions: [^{18}F]-FDG PET/CT is gaining importance in diagnosing and monitoring infectious and inflammatory disorders like PUO, BUO, HIV/AIDS, TB spine, vasculitis, sarcoidosis, spine, and pulmonary infections. It is also a reliable and accurate modality for early diagnosis, quantification of disease burden, and treatment monitoring in this context. The utility and versatility of this precious tracer can be explored further to define its clinical usefulness precisely in the context of infection and inflammation.

The emerging tracers in molecular cardiac imaging

[1]Shrestha BB MBBS, [1]Singh SB MBBS, [1]Shah R MD
Department of Radiology, University of Pennsylvania

Introduction : Cardiovascular disease (CVD) remains the most prevalent cause of death worldwide albeit modern advances in prevention and treatment. Molecular cardiac imaging allows for the noninvasive detection, earlier diagnosis, monitoring of therapies, and better prognostication of CVDs. Most commonly used tracers like [^{18}F]-fluorodeoxyglucose (FDG) and [^{18}F]-sodium fluoride (NaF) have been used in the cases of several CVDs such as atherosclerosis, calcification, myocarditis, myocardial neoplasms and so forth. But with the advent of new radiotracers such as ^{18}F-Labelled tracers, ^{68}Ga-DOTATATE, ^{68} Ga-FAPI, 99mTc-pyrophosphate and β-methyl-*p*-123-I-iodophenyl-pentadecanoic acid (123-I-BMIPP), there has been advancement in molecular cardiac imaging. However, there has not been enough research to identify clinical uses, efficacy, and limitations to explore their significance as cardiac tracers in different imaging modalities.

Objectives: To know about the new radiotracers in cardiac imaging. To describe advantages, disadvantages, and challenges for its routine clinical use in the diagnosis and treatment of CVDs.

Methods: We searched highly cited and latest articles related to emerging tracers in molecular cardiac imaging in Google Scholar and PubMed. We used keywords like "cardiac", "radiotracers", "molecular", "cardiology", and "imaging" to compile the relevant articles. They were thoroughly reviewed, analyzed, and the data was recorded in excel sheets. Finally, the information was organized to construct this comprehensive abstract.

Result: Several cardiovascular disorders have been diagnosed from the introduction of innovative ^{18}F-labelled radiotracers with longer half lives and lower costs. ^{18}F-labelled radiotracer like ^{18}F-flurpiridaz helps in the detection of myocardial blood flow (MBF), improves spatial resolution of the myocardium, and aids in the diagnosis of vascular stenosis. Similarly, ^{18}F-Florbetapir has been used in cardiovascular amyloid disease and ^{18}F-fluciclatide is used in aortic atherosclerosis. The presence of residual activity of these radiotracers, however, can obstruct the display of activity in the heart. Another tracer, ^{68}Ga-DOTATE, facilitates the detection of rare heart metastases, particularly myocardium. However, due to the relative rare occurrence of metastasis, comparative studies using this radiotracer in large populations are lacking. Several PET myocardial perfusion tracers used for assessment (e.g., [82Rb]RbCl, [13N]NH3, and [15O]H2O) produced higher quality images than technetium single photon emission computed tomography (SPECT) imaging. FAPI PET/CT allows the identification of locally defined myocardial remodeling due to immune checkpoint inhibitor (ICI)- associated cardiac inflammation. It contributes to cardiac risk stratification when integrated into cancer stage diagnostics. Further research is needed to determine the predictive usefulness of FAPI PET/CT in diagnosing ICI-associated myocarditis. 99mTc-pyrophosphate (PYP) is used to image transthyretin cardiac amyloidosis which can cause heart failure and left ventricular wall thickening using SPECT/CT. A BMIPP scan may reveal ischemic memory. Moreover, BMIPP SPECT has recently been introduced for assessing myocardial metabolism and ventricular function simultaneously. Furthermore, it is helpful for gaining a better understanding of the pathophysiology of heart failure and cardiomyopathy. However, more research on BMIIP in terms of the use of fatty acid metabolic imaging for the proper diagnosis of ischemic heart disease (IHD) is required.

Conclusion: Although FDG and NaF are commonly used to identify cardiac diseases like atherosclerosis, calcification, malignancy, and so forth, numerous other tracers have been found to be helpful. The rapid evolution of hybrid PET/CT and PET/MR imaging with the advanced tracers has provided a new perspective on cardiac imaging by providing combined anatomic and functional evaluation of coronary disease and alterations in cardiac functions. However, multicenter, randomized prospective studies may be required to elucidate the clinical usefulness of the emerging tracers in molecular cardiac imaging.

VascuViz: a multimodality and multiscale imaging and visualization pipeline for cancer systems biology

Akanksha Bhargava[1] (PhD), Benjamin Monteagudo[2], Priyanka Kushwaha[3] (PhD), Janaka Senarathna[1] (PhD), Yunke Ren[2], Ryan C. Riddle[3] (PhD), Manisha Aggarwal[1] (PhD) & Arvind P. Pathak[1,2,4,5] (PhD)
[1]Russell H. Morgan Department of Radiology and Radiological Science, [2]Departments of Biomedical Engineering, [3]Orthopedic Surgery, [4]Electrical Engineering, and [5]Sidney Kimmel Comprehensive Cancer Center,
The Johns Hopkins University School of Medicine, Baltimore MD

Background: Image-based systems biology is emerging as a powerful new paradigm to better understand the role of blood vessels in cancer progression and therapy. To do this requires a multimodality pipeline that enables ex vivo imaging of tumor vasculature with MRI, CT and optical microscopy and permits integration with other microenvironmental factors at spatial scales spanning several orders of magnitude in the same sample. Therefore, we developed a new pipeline called VascuViz that enables multimodality, multiscale 3D imaging and visualization of the tumor microenvironment (TME) in the same sample for image-based systems biology investigations.

Objective: Tumor vasculature data are often available only from a single modality or at a given spatial scale. Moreover, cross modality data are difficult to integrate often due to lack of common landmarks. Therefore, our objectives are: (1) to develop an easy-to-use sample preparation and imaging workflow that makes tumor vasculature visible across MRI (50 μm), CT (8 μm) and optical microscopy (< 1 μm) using a single blood vessel labeling step that permits concurrent acquisition of complementary contrast mechanisms; and (2) leverage this cross-modality visibility of blood vessels for multiscale integration and characterization of the TME in the same sample.

Methods: An MDA-MB-231 breast tumor bearing Ncr-nu/nu mouse was perfused with an intravascular polymer consisting of BriteVu® (BVu) and Galbumin™-Rhodamine (GalRh) contrast agents. After fixation, tumor was excised and imaged on a 9.4 T MRI scanner using T1- and DW- sequences at 40 μm from which apparent diffusion coefficient (ADC) and fractional anisotropy (FA) maps were computed. Next, CT data was acquired at 9 μm. Following this, 3D vasculature and green fluorescent protein (GFP) expression from cancer cells were imaged using a multiphoton microscope (MPM) and fibrillar collagen (Col) expression using second harmonic generation (SHG) imaging (< 1 μm). Finally, multiscale TME data were integrated in 3D using a vascular-fiducials based image co-registration approach [Bhargava et al, Nat Methods 2022].

Results: VascuViz enabled multimodality 3D imaging and visualization of the TME from the macroscopic whole-tumor scale to the mesoscopic vascular network scale, down to the microscopic scale of individual cancer cells without requiring any additional sample processing for MRI, CT or MPM/SHG (**Fig. 1a-h**). Co-registration between multiscale imaging data (**Fig.i-l**) revealed that CT-derived intervessel distance (EDM) was positively correlated with MRI-derived ADC and inversely correlated with SHG-derived Col fractional area and MRI-derived FA, while FA and Col fractional area were also positively correlated (**Fig. 1m-p**) ($p < 0.05$). These TME distributions were suggestive of efficacious drug delivery from 0.1- 0.5 mm from the tumor boundary in contrast to intermediate to potentially poor delivery from 0.5 to 2.5 mm due to elevated barriers to convective and diffusive transport in this breast cancer xenograft (**Fig. 1q-t**).

Conclusions: VascuViz provided a new multiscale 3D imaging and visualization pipeline using MRI, CT and optical microscopy for cancer systems biology. We hope that this multiscale pipeline will have a broad applicability in image-based systems biology investigations of healthy tissues (e.g. brain) and other vascular diseases (e.g. stroke).

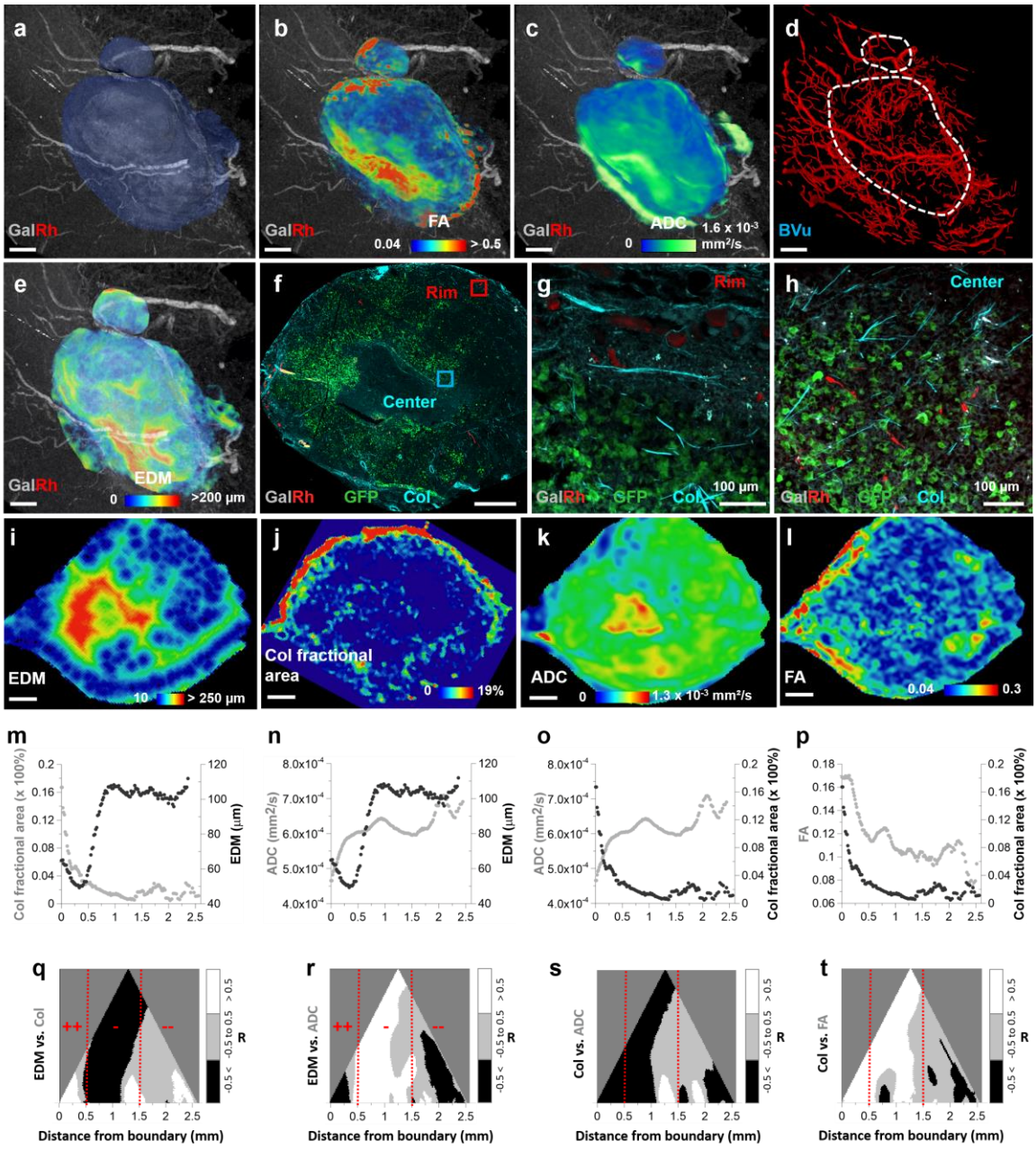

Fig. 1: VascuViz enabled multiscale characterization of the TME in a human breast cancer xenograft: (a-h) Multiscale imaging data was derived from a GalRh-BVu perfused MDA-MB-231 breast tumor xenograft using the VascuViz pipeline. This included **(a)** soft tissue contrast and vascular data from T1W MRI (40 µm), **(b-c)** tissue structure and cellularity data from DW-MRI (50 µm), **(d-e)** microvasculature and corresponding EDM data from high-resolution CT (9 µm) and **(f-h)** 3D optical microscopy derived data (< 1 µm) for capillaries (red), GFP from cancer cells (green) and fibrillar Col from SHG imaging (blue). Next, EDM (**i**), Col (**j**), ADC (**k**) and FA (**l**) data were integrated using a vascular fiducial based coregistration approach. This enabled the generation of scatter plots illustrating the mean tumor boundary-to-center profiles of Col w.r.t EDM (**m**); ADC w.r.t EDM (**n**); ADC w.r.t Col (**o**) and FA w.r.t Col (**p**); and generation of hierarchical correlation plots (**q**–**t**) revealing potential regions of efficacious drug delivery (++), intermediate efficacy of delivery (−) and poor drug delivery (−) in the same tumor.

Downfield proton MR spectroscopic imaging of the brain at 3T with 3D coverage

İpek Özdemir Ph.D.[1], Sandeep Ganji Ph.D.[2], Joseph Gillen B.S.[1,3],
Michal Považan Ph.D[4], and Peter B. Barker, D.Phil. [1,3]
[1]Department of Radiology, JHU SOM, Baltimore, MD, [2]Philips Healthcare, Best, The Netherlands, [3]Kennedy Krieger Institute, Baltimore, MD, [4]Danish Research Center for MR, Copenhagen, Denmark

Background

In proton MRS of the human brain, signals occur both upfield and downfield from the water resonance. Most studies to date have focused on the large upfield resonances, but there have also been some studies of the downfield peaks, usually using single voxel spatial localization. Recently, a single slice, 2D MRSI study of the downfield resonances in normal human brain was published at a nominal spatial resolution of 1.5 cm^3 (1).

Objective

The objective of the current study was to develop a 3D downfield MRSI protocol with near full brain coverage and high spatial resolution at 3T.

Methods

Testing was performed in a normal human volunteer (M, 57 yr.) using a Philips 3T Elition scanner equipped with a 32-channel receive head coil. A 3D, circularly phase-encoded version of the previously developed 2D MRSI sequence (1) with 1331 spectral-spatial excitation and frequency selective refocusing was implemented (Fig. 1). Scan parameters were TR/TE 287/22 ms, flip angle 78˚, FOV 200x180x120 mm, matrix size 29x26x8, nominal voxel size 7x7x15 mm ≈ 0.7 cm^3, 100mm slab excitation, 1 NEX, scan time 22m 40s. The 1331 pulse delay (d) was set to give maximum excitation at 7.4 ppm, and frequency-selective refocusing was achieved using a sinc-Gauss 180˚ pulse applied at 7.8 ppm (11ms, 400 Hz BW). An inferior saturation pulse was also applied. Data were post-processed using the 'csx3' program, and images of the 8.1ppm amide proton resonance created by numerical integration.

Results

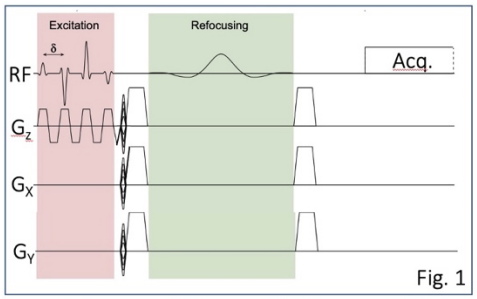

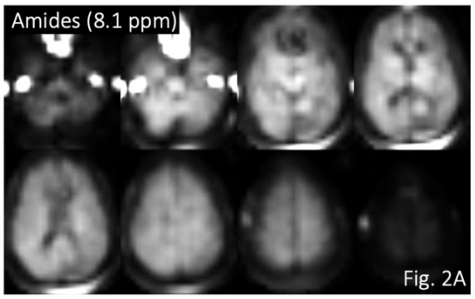

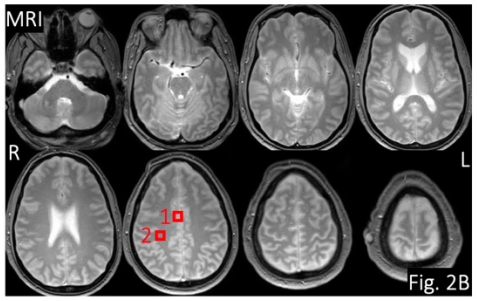

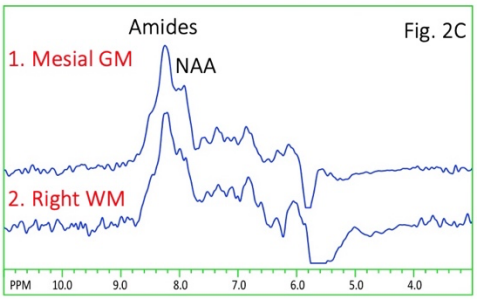

Fig. 2A shows images of the 8.1 ppm amide resonance from all 8 slices, as well as corresponding localizer MR images (Fig. 2B). Also shown are representation spectra (Fig. 2C) and corresponding voxel locations from 2 regions of interest illustrated in Fig. 2B.

Conclusions

Downfield MRSI with 3D coverage is achievable at 3T in a clinically feasible scan time. Compared to upfield MRSI, some of the technical advantages include the ability to use short TR (due to the 'relaxation enhancement' effect), no need for additional water or lipid suppression, and also slightly less sensitivity to field inhomogeneity, since the downfield resonances have broader intrinsic linewidths compared to upfield. Scan time reductions should be possible in the future using fast MRSI techniques, such as EPSI readouts or parallel imaging. Downfield MRSI may give specific metabolic information on slowly exchanging molecules that is complementary to that observed using CEST MRI, which is more sensitive for intermediate exchange rates.

References

1. Povazan M, Schar M, Gillen J, Barker PB. Magnetic resonance spectroscopic imaging of downfield proton resonances in the human brain at 3 T. Magn Reson Med 2022;87(4):1661-1672.

Hyperpolarized [1-^{13}C]Pyruvate Dynamic Metabolic Imaging of Murine Prostate Cancer Model to Investigate the Metabolic Association with Androgen Sensitivity

Aditya Jhajharia[1], Dexue Fu[2], Minjie Zhu[1], Shu Wang[2], Ian Qian[2], Aidan Kennedy[2], M. Minhaj Siddiqui[2,3,4], Dirk Mayer[1,3]

[1]Department of Diagnostic Radiology and Nuclear Medicine, University of Maryland, Baltimore, USA. [2]Division of Urology, Department of Surgery, [3]Greenebaum Cancer Center, University of Maryland School of Medicine, Baltimore, MD, USA; [4]The Veterans Health Administration Research and Development Service, Baltimore, MD, USA

Background: Increased level of pyruvate to lactate conversion is associated with the aggression of the tumor in preclinical studies. Hyperpolarized magnetic resonance spectroscopic imaging (MRSI) can be used to access the real time pyruvate metabolism by enhancing ^{13}C MR signal by a factor up to five-orders of magnitude *in vivo*.

Objective: The purpose of this study is to investigate the metabolomic signature differences associated with androgen sensitivity in murine model of prostate cancer.

Methods: Androgen-dependent (LNCaP) and androgen-independent (CSS90) cancer cell lines were used to generate tumors into mice. A clinical 3 T GE 750w MRI scanner was used to acquire the metabolic imaging data using a fast 3D spiral chemical shift imaging (spCSI) sequence. Tumor slices were analyzed by using Seahorse XF bioenergetics analyzer to measure oxygen consumption rate (OCR) and extracellular acidification rate (ECAR).

Results and Conclusions: We utilize hyperpolarized MRSI to compare the different metabolic signature for androgen dependent and androgen independent tumor type. *In vivo* hyperpolarized imaging reports that pyruvate to lactate conversion is significantly higher in CSS90 than LNCaP tumors. ECAR measurements show higher glycolytic behavior of CSS90 compared to LNCaP tumor slices, which is consistent with *in vivo* findings. After treatment with MDV3100, reduced pyruvate to lactate conversion and higher oxidative phosphorylation in LNCaP tumors could be an indication of a positive response to targeted therapy. These findings indicate an effect after treatment with MDV. This study suggests that hyperpolarized [1-^{13}C]pyruvate imaging is a useful means to characterize the tumor type specific differences and can potentially access the responses to therapies.

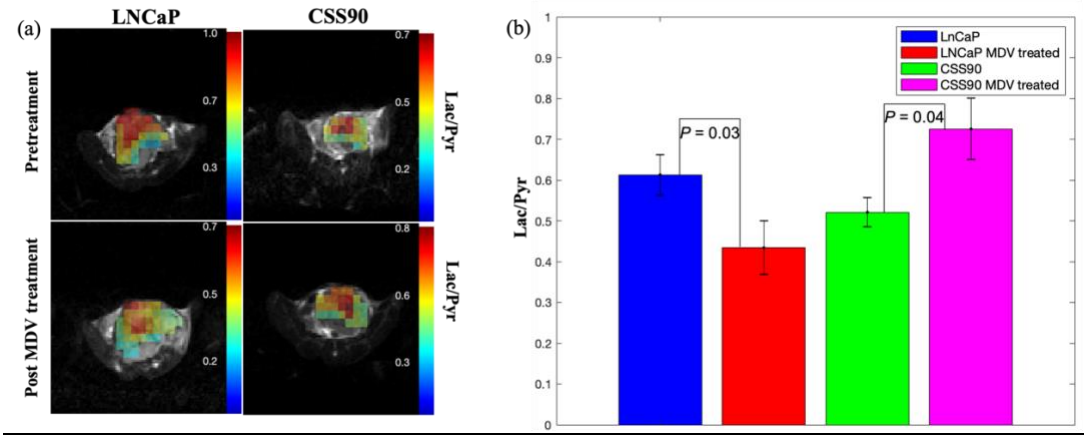

Fig (a) ^{13}C metabolic maps of lactate over pyruvate (Lac/Pyr) superimposed on corresponding proton MR images of PCa mice with LNCaP and CSS90 tumors before and post-MDV treatment. These metabolic images are averaged over all 16 time points acquired with dynamic 3D spCSI. Color scale of Lac/Pyr images show the magnitude of the lactate over pyruvate ratio. (b) average lactate-to-pyruvate ratios for tumors LNCaP and CSS90, before and after MDV treatment with standard errors.

Comparative studies on the optimal liposome fusion protocol for preparing hybrid extracellular vesicles for drug delivery and imaging

Safiya Aafreen[1,2,3], Wenshen Wang[1,2], Aline Thomas[1,2], Guanshu Liu[1,2]
1 F.M Kirby Center, Kennedy Krieger Institute, 2 Department of Radiology, Johns Hopkins University, 3 Department of Biomedical Engineering, Johns Hopkins University

Background Increasing evidence shows that extracellular vesicles (EVs) are highly advantageous as a natural nanoparticle system for drug and gene delivery.(Armstrong and Stevens 2018) EV-based therapy may open a new avenue for treating formidable CNS diseases such as multiple sclerosis (MS).(Nuzzo and Picone 2021) A number of methods have been developed to load therapeutic or imaging agents into EVs.(Hettich et al. 2021) Among them, the strategy of using membrane fusion with liposomes has been shown to be highly effective to augment cargo uptake into EVs (**Fig. 1A**). However, a systemic comparison of different fusion methods in terms of loading efficiency and the impact of EV functionality has not been performed.

Objective To compare three membrane fusion strategies, including freeze-thawing, PEG-mediated fusion, and extrusion, for preparing hybrid EV particles for EV-based therapy and in vivo MRI tracking.

Method Model liposomes were prepared using the thin-film hydration and extrusion method (Chen et al. 2019) with a formulation of PC:PE:DOTAP = 23:17:10 (w/v). Tumor cell-derived EVs were isolated from conditioned culture media of KPC pancreatic cancer cells (Han et al. 2019). Three liposome-EV fusion methods were conducted according to previously published protocols, including a) freeze-thaw(Sato et al. 2016), b) extrusion (Hu et al. 2021), and c) PEG-mediated fusion (Piffoux et al. 2018) at a 1:1 ratio between liposomes and EVs. To assess the efficiencies to load therapeutic or imaging agents, fluorescent FITC-dextran (150 kDa) or SPIO (core size = 5 nm) were encapsulated into liposomes in the re-hydration step during liposome preparation. To assess the ability to fuse with the recipient cells for gene delivery, GFP plasmid (pcDNA3-EGFP, Addgene) was loaded. The sizes of hybrid EV particles were assessed using DLS and NTA; fusion efficiency was assessed using the FRET method (Thorsteinsson et al. 2020); loading efficiency was assessed using fluorescence imaging and magnetic particle imaging; the functionality was assessed by the GFP expression after the incubation of hybrid EVs with KPC cells for 12 hours. Finally, in vivo MRI tracking ability was tested in an MS mouse model within the first 30 minutes after iv injection of $2x10^9$ hybrid EVs.

Results The FRET results show that all fusion methods could result in liposome EV fusion, while the PEG-mediated fusion method provided the highest fusion efficiency. Increased particles sizes were observed in all methods, with only the extrusion method showing a minimal size change and the most homogenous size distribution. Judged by the fluorescence intensity of the encapsulated FITC-dextran and MPI signal of the encapsulated SPIO in the final product, PEG-mediated fusion provided the highest loading efficiency. The PEG method also led to the highest gene transduction rate, as visible from the GFP-expressing cells. Finally, the SPIO-loaded hybrid EV particles allowed the in vivo tracking after systemic injection in the mice with MS, showing a good spatial correlation with the lesions highlighted in Gd-enhanced MR images (**Fig. 1B**).

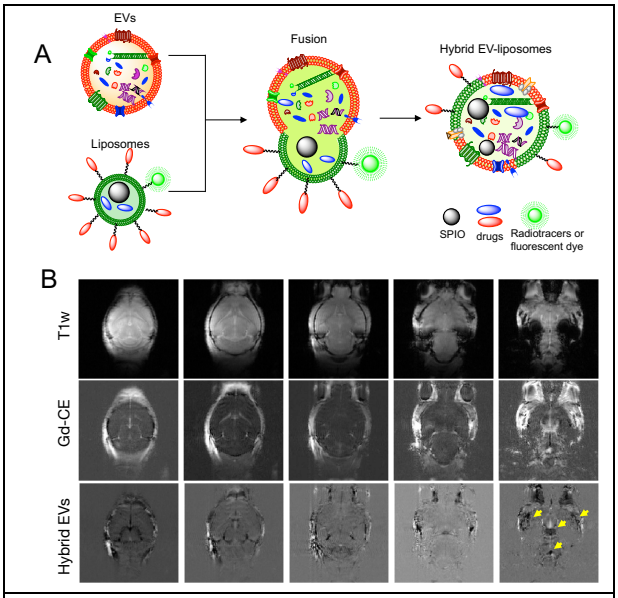

Figure 1. (**A**) illustration of loading therapeutic and imaging agents to EVs by fusing them with preloaded liposomes. (**B**) In vivo tracking of hybrid EVs in a representative mouse with MS. Yellow arrows indicate the hypointense areas as a result of uptake of SPIO-loaded hybrid EVs.

Conclusion We comprehensively compared the loading efficiency and impact on EV functionality of different liposome fusion methods. Among them, PEG-mediated fusion exhibited many desirable properties and has allowed preparing hybrid liposome-EV particles for efficient drug delivery and MRI tracking in vivo.

Funding Support: R33HL161756; Reference Armstrong JPK, Stevens MM (2018). Adv Drug Deliv Rev 130:12-16; Nuzzo D, Picone P (2021). International Journal of Molecular Sciences 22 (16):8866; Hettich BF, Bader JJ, Leroux JC (2021). Advanced Healthcare Materials 10.1002/adhm.202100047:2100047; Chen Z, Li Y, Airan R et al. (2019). Quant Imaging Med Surg 9 (9):1579-1591; Han Z, Zhang S, Fujiwara K et al. (2019). Bioconjug Chem 30 (5):1425-1433; Sato YT, Umezaki K, Sawada S et al. (2016). Scientific Reports 6 (1):21933; Hu M, Zhang J, Kong L et al. (2021). ACS Nano 15 (2):3123-3138; Piffoux M, Silva AKA, Wilhelm C et al. (2018). ACS Nano 12 (7):6830-6842; Thorsteinsson K, Olsén E, Schmidt E et al. (2020). Analytical Chemistry 92 (23):15336-15343

Radionuclide study of bacterial translocation of labeled Escherichia coli in rats after asplenization.

S.A. Lepekhova [1], T.M. Andaeva [2], Yu.M. Galeev [1], P.O. Inozemtsev [1], T.A. Gurepka [1], G. Qiao [3]

[1]Irkutsk Scientific Center of Siberian Branch of the Russian Academy of Sciences

[2]Irkutsk Regional Clinical Hospital

[3]Department of Diagnostic Radiology and Nuclear Medicine, School of Medicine, University of Maryland at Baltimore

Background. Increased susceptibility to pathogens of infectious diseases, an increase in the frequency of purulent-inflammatory complications in the early postoperative period after asplenia.

Objective. Evaluate the bacterial translocation of labeled Escherichia coli by scintigraphy.

Methods. The study was carried out at the Department of Medical and Biological Research and Technology of the Institute of Scientific Centers of the Siberian Branch of the Russian Academy of Sciences. In the experiment, 6 healthy and 42 asplenized rats were used. The study of bacterial translocation from the lumen of the small intestine was performed by scintigraphy (in dynamic and static modes) using a bacterial radiopreparation - 99mTc-labeled E. coli bacteria, prepared according to the original method in healthy animals and on day 6 after asplenization.

Results. Using static gamma scintigraphy, it was found that splenectomy promotes bacterial translocation (accumulation of labeled bacteria in the liver area), the results indicate liver damage, the source of which is bacterial translocation.

Conclusions. The assessment of bacterial translocation of labeled Escherichia coli by scintigraphy revealed that liver damage develops under conditions of asplenia, pathogenesis is associated with bacterial translocation of microflora into the portal vein system.

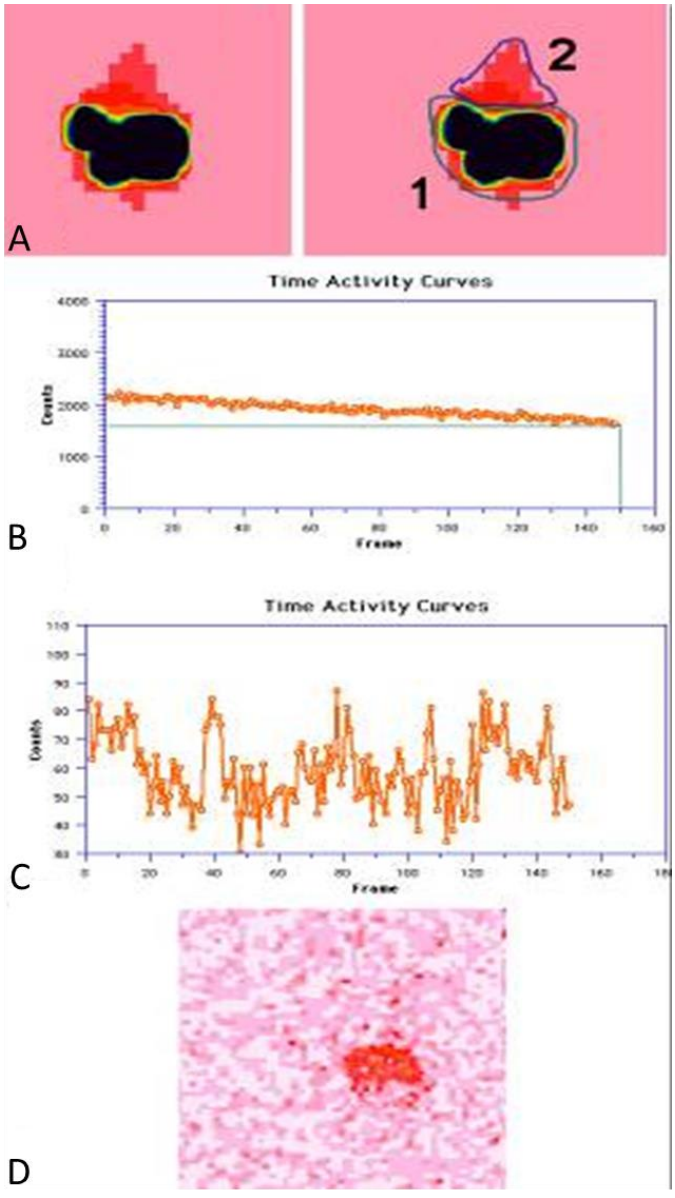

Figure 1. Picture. Radionuclide study of the effect of asplenization on the processes of bacterial translocation of labeled Escherichia coli in rats. Animals on the 6th day after asplenization.
A - summation frame obtained for 2.5 hours of the study. On the right - the same frame with outlined areas of interest: the abdominal cavity (1) and extra-abdominal lesions (2). B – activity-time curves from projection 1: monotonic decrease in radioactivity throughout the study. The number of impulses in the last minute was 75% of the initial activity, which corresponds to the decay of technetium (bacterial translocation was not registered). C – "activity-time" curves from projection 2. The activity slightly differs from the background. D - static gamma scintigraphy for 10 minutes after excision of the intestine (center of maximum radioactivity). Accumulation of activity in the projection of the liver in rats.

A two-photon microscope with high-speed volumetric imaging and photostimulation modules for preclinical studies

Yajie Liang, Guangda Qiao, Anna Jablonska, Miroslaw Janowski, Piotr Walczak

Department of Diagnostic Radiology and Nuclear Medicine, University of Maryland Baltimore, USA.

Background: Two-photon (2p) microscope has been increasingly used for neurobiology and neurophysiological studies(Zipfel, Williams et al. 2003). However, its application in preclinical studies has not been popular, especially advanced modules in 2p microscope which are largely limited to a small field of optical engineering or neuroscience labs.

Objective: We aim to build a 2p microscope with advanced modules: volumetric imaging and optostimulation (**Fig. 1**) for preclinical studies in the brain, such as stroke and brain cancer. This will enable the exploration of the pathogenesis or efficacy of therapeutics at unprecedented perspectives.

Methods: Designed by Janelia Research Campus (JRC) of Howard Hughes Medical Institute, the Modular In Vivo Multi-photon Microscope 2 (MIMMS2.0) was first built through contracting with optical engineers from JRC. Then a second laser scan head was installed to allow simultaneous stimulation through another laser beam (fixed wavelength at 1040 nm) while imaging. This makes it possible to perform optogenetic interventions while recording the activity or morphology of a group of cells in live animals. Finally, a volumetric imaging module will be added. Understanding the structure and function of vasculature or brain cells in the brain requires the observation of distributed hemodynamics at high spatial and temporal resolution in three-dimensional (3D) volumes in vivo. But this is not possible using conventional 2p imaging method. As we have demonstrated in our publication(Lu, Liang et al. 2020), we will use Bessel focus for laser scanning, achieving high throughput monitoring of hemodynamics or neuronal activity in the brain of live animals.

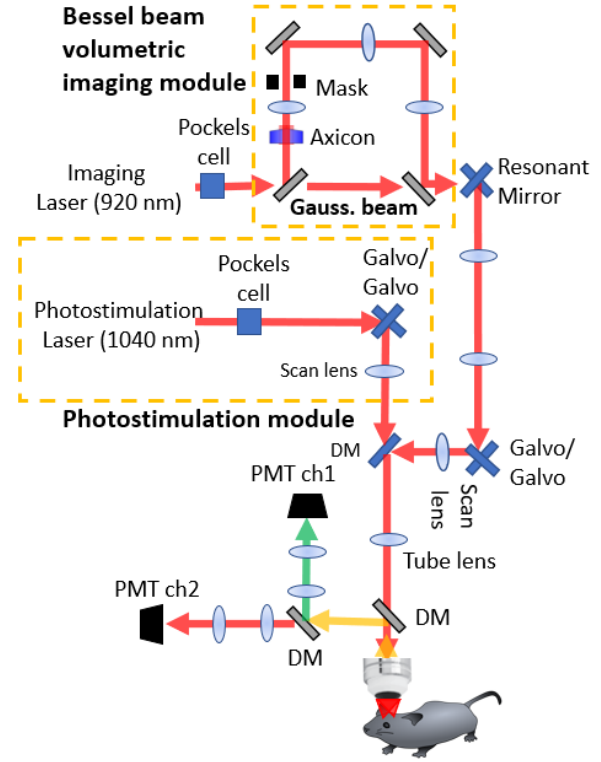

Figure 1. The optical path in our advanced 2p microscope with the photostimulation and volumetric imaging modules added to the MIMMS2.0. DM: Dichroic mirror; Gauss. beam: Gaussian beam; PMT: Photomultiplier.

Results: MIMMS2.0 was built and upgraded with the optogenetic stimulation module, allowing simultaneous imaging and interventions. Systematic characterization was performed, and we have confirmed its performance of basic imaging functions such as acquiring 3D stacks, multi-focus imaging and blood flow-speed tracking. Next step is to install the volumetric imaging module based on Bessel beam, which enables us to observe cellular events within a 3D space at high temporal resolution.

Conclusion: We presented here a 2p microscope with powerful modules for preclinical studies. The aim is to upgrade MIMMS2.0 to an advanced UMB version with high-speed volumetric imaging and photostimulation capacities.

Reference

Lu, R., Y. Liang, G. Meng, P. Zhou, K. Svoboda, L. Paninski and N. Ji (2020). "Rapid mesoscale volumetric imaging of neural activity with synaptic resolution." Nat Methods **17**(3): 291-294.

Zipfel, W. R., R. M. Williams and W. W. Webb (2003). "Nonlinear magic: multiphoton microscopy in the biosciences." Nature Biotechnology **21**(11): 1369-1377.

The quest to improve efficacy of endovascular neuro-interventions: focus on spatial precision of the blood brain barrier opening in a mouse model

G. Qiao [1], M. Walczak [2], Y. Liang [1], A. Jablonska [1], M. Janowski [1], P. Walczak [1]

[1]Department of Diagnostic Radiology and Nuclear Medicine, School of Medicine, University of Maryland Baltimore

[2]University of Maryland Baltimore County

Background. The brain is by far the most difficult target for drug delivery. Vast majority of systemically injected drugs do not reach therapeutic concentrations in the brain. As a consequence, virtually all promising drugs for brain diseases failed in clinical trials [1]. As most therapeutic agents do not cross the blood–brain barrier (BBB), transient BBB opening (BBBO) is one strategy to enable delivery into the brain for effective treatment of CNS disease [2]. Among the available drug delivery routes intra-arterial (IA) delivery stands out with several unique advantages including the generation of high tissue concentrations at a specific site, low systemic exposure, and availability of techniques for reversible BBB opening [3, 4]. These obvious benefits have spurred clinical translation, but although IA drug delivery with BBBO has been used for decades in the treatment of brain tumors, the efficacy of therapies is still limited. To better understand obstacles and improve efficacy, IA drug delivery need to be systematically studied in mice, exploiting the benefits of the guidance of magnetic resonance imaging (MRI) and intravital microscopy. However, due to small size of cerebral vasculature IA catheter is placed proximally within carotid arteries precluding spatial control over the territory of the brain targeted by the injection. We also observed inconsistent or rather ineffective perfusion of cerebral cortex from bolus injections into the common carotid artery (CCA). That in turn complicates intravital microscopy studies limited to superficial structures of the cerebral cortex.

Objective was to test the hypothesis that fully occlusive catheterization of the CCA and resulting re-routing of cerebral circulation restricts brain volume perfused by the catheter to deep brain structures. In contrast, less disruptive catheterization by accessing the external carotid artery (ECA) results in broader perfusion.

Methods. Male C57BL6 mice (10-12 weeks of age) were subjected to catheterization of ECA or CCA for injection into the internal carotid artery (ICA). Mice with IA catheter were placed in 9.4T MRI (Bruker) for image-guided neurointervention. Gadolinium (Gd) (1mM) was administered using infusion pump at the rate ranging between 150-500ul/min. Dynamic contrast-enhanced (DCE) and gradient-echo echo planar imaging (GE-EPI) sequences were used to dynamically assess brain perfusion territory. Mannitol (25%) was injected IA over 30s at pre-determined speed to open the BBB and DCE with intra-venues (IV) bolus of Gd (0.1mmol/kg) being used to determine BBB integrity for calculation of vascular permeability constant (k-trans).

Results. IA delivery via CCA resulted in perfusion of restricted brain territory, primarily hippocampus and the thalamus (**Fig.1 A**). When catheter was placed in the ECA trans-catheter perfusion was directed to nearly entire hemisphere with significantly larger brain territory (**Fig.1 B**, quantified in **Fig.1 C**; $p \leqslant 0.05$). Importantly ipsilateral cortex was consistently perfused. This spatially selective perfusion territory was in good agreement with brain region with open BBB following Mannitol injection (**Fig.1 D, E**). In none of the animals we did not observe hemorrhages or lasting neurological deficits.

Conclusions. We have shown that by selecting ECA vs. CCA it is possible to achieve more spatial selectivity in mice and that for targeting cerebral cortex ECA catheterization is a method of choice.

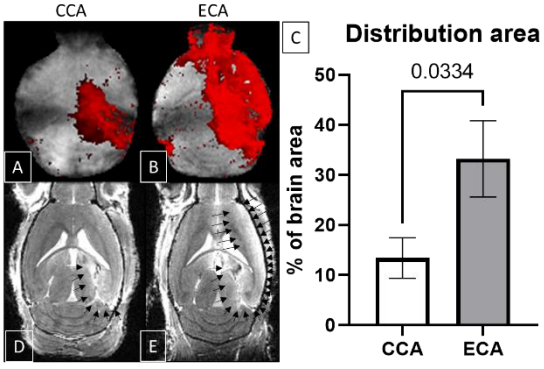

Figure. 1

1. Del Zoppo, G.J., *Why do all drugs work in animals but none in stroke patients? 1. Drugs promoting cerebral blood flow.* J Intern Med, 1995. **237**(1): p. 79-88.

2. Linville, Raleigh M., et al. *"Modeling Hyperosmotic Blood–Brain Barrier Opening within Human Tissue-Engineered in Vitro Brain Microvessels." J. Cereb. Blood Flow Metab., 2020. **40**(7): p. 1517–1532*

3. Dedrick, R.L., E.H. Oldfield, and J.M. Collins, *Arterial drug infusion with extracorporeal removal. I. Theoretic basis with particular reference to the brain.* Cancer Treat Rep, 1984. **68**(2): p. 373-80.

4. Chu, C., et al., *Hyperosmolar blood-brain barrier opening using intra-arterial injection of hyperosmotic mannitol in mice under real-time MRI guidance.* Nat Protoc, 2022. **17**(1): p. 76-94.

Resting-state based Cerebrovascular Reactivity (CVR) mapping at high spatial resolutions

Lincoln Kartchner MSE.[1], Dengrong Jiang PhD[2], Parimal Joshi MSE[1], Cuimei Xu MS[2], Hanzhang Lu PhD[2], Peiying Liu PhD[1]

[1]Department of Diagnostic Radiology & Nuclear Medicine, University of Maryland School of Medicine

[2]Department of Radiology, Johns Hopkins University School of Medicine

Background: Cerebrovascular reactivity (CVR), an index of the dilatory capacity of cerebral blood vessels, is an important measure of brain health. CVR is typically assessed by coupling a vasoactive stimulus, such as breath-holding or carbon dioxide inhalation[1], with blood-oxygen level-dependent functional MRI (BOLD fMRI). The extra setup, equipment required and level of subject cooperation needed render these traditional methods of limited applicability. Recently, resting-state (RS) BOLD fMRI has been shown capable of generating CVR maps independent of a vasoactive stimulus and comparable to those produced using traditional methods by exploiting the natural fluctuations in the BOLD signal due to inherent variations in breathing patterns[2,3].

Objective: To investigate whether RS-BOLD fMRI based methods can be used to generate CVR maps at high spatial resolutions without any degradation in image quality or correspondence with traditional methods, we collected RS-BOLD scans at three resolutions of decreasing voxel size, and compared the resulting CVR maps against maps generated using a traditional CO2-inhalation coupled BOLD scan.

Methods: Image acquisition: Data were collected from 8 participants (3F/5 M, 26.5 ± 5 years) using a 3T Prisma Siemens scanner with a 32-channel head coil. Four BOLD scans were acquired in each subject: 3 10-minute RS-BOLD scans (2mm, 2.4mm and 3mm isotropic resolutions), and 1 5-minute CO2-inhalation coupled BOLD scan (2mm isotropic resolution. Image analysis: The RS and CO2-inhalation BOLD data were processed using methods described previously[4]. Briefly, data preprocessing included motion correction, linear detrending, spatial smoothing and temporal filtering creating a whole-brain averaged BOLD time course[3]. In RS data, this whole-brain average was used as the independent variable in a regression analysis with linear drift and motion vectors as covariates and the voxel-wise BOLD signal as the dependent variable. In CO2-inhalation data, the end tidal CO2 was shifted to find the maximum correlation with the whole-brain averaged BOLD time course and this shifted EtCO2 was used as the independent variable in a similar voxel-wise regression[5]. The resulting CVR index maps were then normalized to the whole-brain average to yield relative CVR maps. Statistical analysis: Accuracy was measured using Pearson's R^2 and intraclass correlation. Sensitivity was measured by comparing the distributions of Z-scores, derived via the maps of t-values corresponding to the voxel-wise regressions. Reproducibility was assessed by dividing each 10-minute RS-BOLD scan into two 5-minute halves, generating CVR maps and measuring the spatial correlation between the two.

Results: Figure 1a shows the CVR maps obtained from each scan for each subject. Visual inspection suggested that all resolutions can produce good quality maps, with clear grey/white matter contrast. Figure 1b shows the accuracy comparisons. The 2.4mm isotropic resolution RS-CVR maps showed the highest overall spatial correlation and intraclass correlation with the CO2-inhalation CVR maps, nonetheless no significant differences were observed. Figure 1c shows the distribution of mean Z-scores, and a clear pattern of increasing Z-scores with increasing voxel size, likely due to the higher SNR expected with a larger voxel size[6]. Finally, figure 1d shows the spatial correlation between CVR maps generated using the first and second halves in each resolution. Again, the 2.4 mm isotropic resolution had the highest overall correlations, but no significant differences were seen.

Conclusions: In this study we found that RS-CVR mapping is feasible at high resolutions. These results suggest that the RS-CVR mapping method can be used across a range of resolutions, increasing its applicability both to previously collected data, as well as to future basic science and clinical applications.

References: 1. Sleight et al. Front Physiol. 2021 Feb; 12:643468 2. Liu et al. Neuroimage. 2017 Feb 1;146:320-326. 3. Golestani et al. Neuroimage. 2016; 138:147-163. 4. Liu et al. Radiology. 2021 May; 299(2):419-425. 5. Lu et al. J Vis Exp. 2014 Dec 17;(94):52306. 6. Huettel et al. Functional Magnetic Resonance Imaging. 2014, 259-262

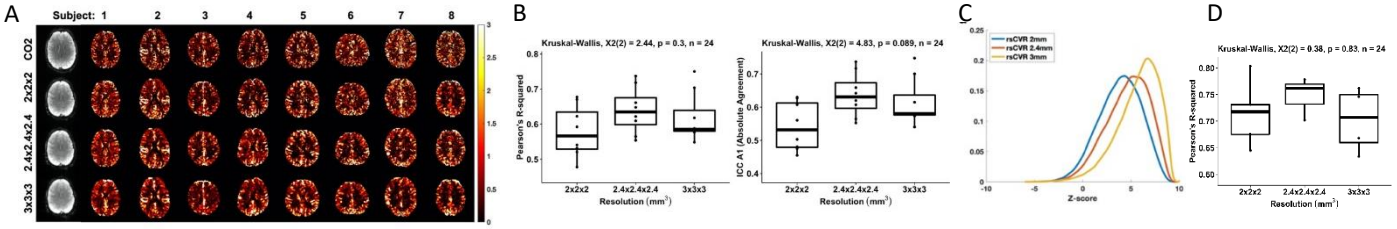

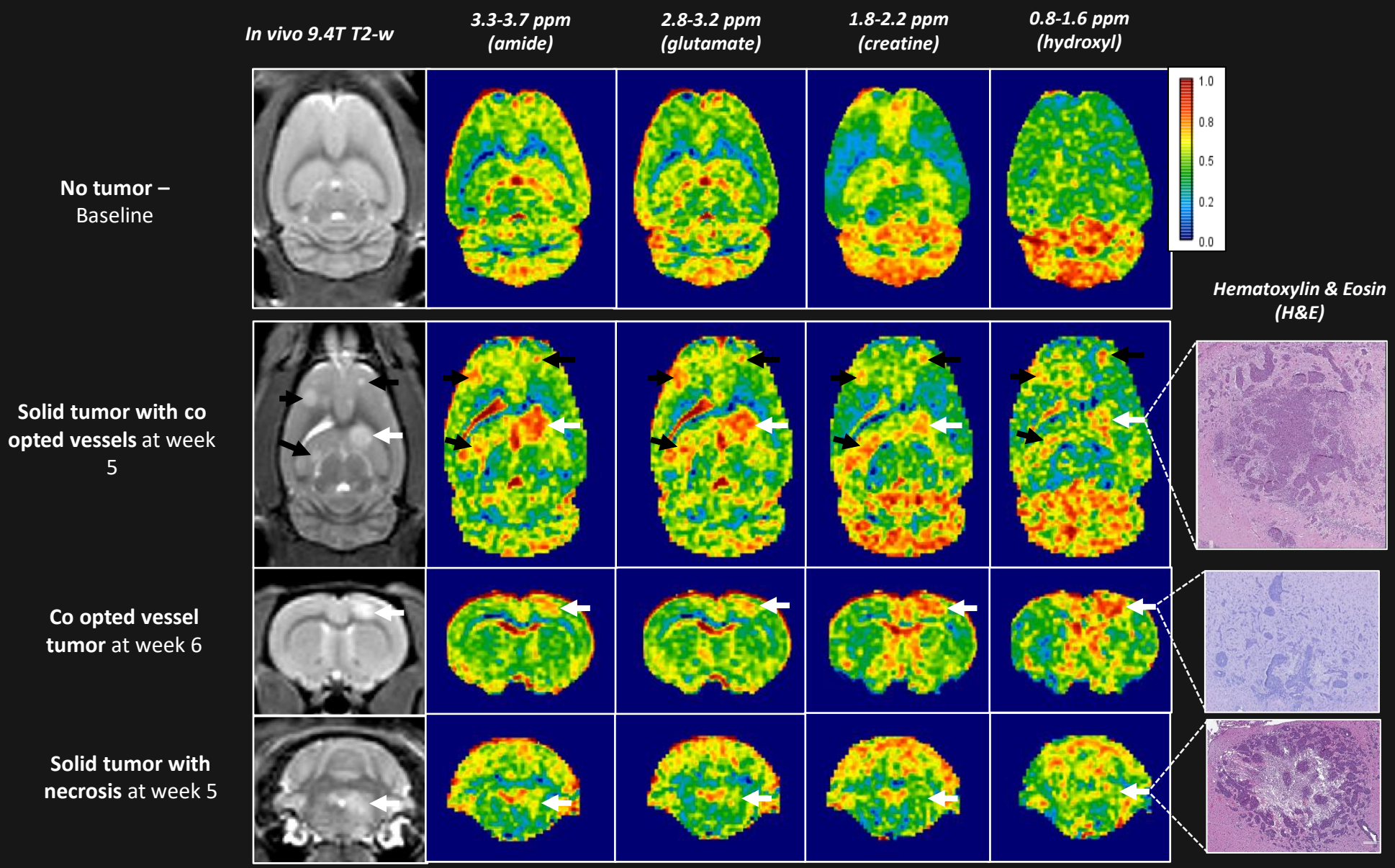

Figure caption: In vivo CEST contrast at 9.4T in rat brains at baseline, 5- and 6-weeks post cancer cells injection with their corresponding T2 weighted and H&E staining.

Title: In vivo metabolic CEST contrast in brain tumors in a model of metastatic breast cancer

Authors: Jennifer Lefeuvre[1] PhD, Katie MacKey[1] BS, Tsang-Wei Tu[2] PhD, Joseph Frank[1] MD
1: Laboratory of Diagnostic Radiology Research, Clinical Center, NIH
2: Molecular Imaging laboratory, Department of Radiology, Howard University College of Medicine

Background: Metastatic breast cancer is known to have a high prevalence of brain metastases with poor patient survival. Brain metastasis are very heterogenous (solid tumor vs co-opted vessel, leaky vs closed blood-brain tumor barrier) and macro-metastases are only detected in the late stage using anatomical MRI. However, metabolic changes may occur earlier and/or may help distinguish different type of tumors. Glucose and glutamate are one of the most used nutrients by tumor cells and has been successfully imaged using the relatively recent new technique chemical exchange saturation transfer (CEST).

Objective: Here, we investigate the metabolic changes using CEST MRI to characterize hematogenous-induced metastatic breast cancer in the brain over time.

Methods: Nude rats were intracardiacally injected with MDA-MB231 brain seeking breast cancer cells. CEST MRI was acquired at 9.4T on 3 slices using saturation pulse with 31 frequency offsets (+/- 6 ppm) followed by T2-w RARE sequence. CEST maps were obtained from the MTR_{asym} curves: 0.8-1.6ppm (hydroxyl), 1.8-2.2 ppm (creatine), 2.8-3.2 ppm (glutamate), 3.3-3.7 ppm (amide). Each CEST map was normalized to the whole brain intensity to get the tumor signal changes to the contralateral normal-appearing brain. A total of 30 tumors were analyzed across 13 animals. Hematoxylin and Eosin (H&E) was performed on selected tumors to classify tumor phenotypes (vessel co-opted tumor, solid tumor with co-opted vessel, solid tumor with necrosis and pure solid tumor).

Results: Nude rats developed metastatic brain tumors on the selected MRI slices between weeks four and five post injection and corresponded to the appearance of CEST signals. Brain metastases demonstrated differences in metabolite levels which was not associated with the hyperintense signal on T2w images. Tumors with areas of necrosis had little or no CEST contrast compared to solid metastases and tumors co-opting vessel that showed increased CEST contrast across metabolites. Significant differences between tumors and contralateral brain were seen at 4- and 5-weeks across all four metabolites of interest ($p \leq 1.9 \times 10^{-5}$). No significant difference was found for the CEST contrast intensity across tumor phenotypes for all four metabolites.

Conclusion: The investigation of MDA231 breast cancer brain metastases in the nude rat was evaluated with CEST MRI for metabolic changes for the first time. Our results indicate that hematogenous induced breast cancer brain metastasis CEST contrast may vary with the degree of tumor formation providing the ability of monitoring potential response to treatment. In this study, most of the analyzed tumors were co-opting vessels with or without solid tumor on histology. Further research will involve the optimization of CEST parameters to differentiate better different metabolites across tumors.